Applied Catalysis A, General 704 (2025) 120400

Contents lists available at ScienceDirect

Applied Catalysis A, General

journal homepage: www.elsevier.com/locate/apcata

Investigation of oxygen mobility on LaNi-Zn perovskite catalyst for carbon inhibition in dry reforming of methane

Juliana Bertoldi [a,*], Camila E. Kozonoe [a,b], Éder V. Oliveira [a], Morgana Rosset [a], Larissa Otubo [b], Elisabete M. Assaf [c], Martin Schmal [a,*]

[a] Laboratory for Research and Innovation in Catalytic Processes - LaPCat, Department of Chemical Engineering, Polytechnic School, University of São Paulo, Cidade Universitária, Av. Prof. Lineu Prestes, 580, Bl.18, São Paulo, SP 05508-000, Brazil
[b] Instituto de Pesquisas Energéticas e Nucleares, IPEN/CNEN-SP, Cidade Universitária, Av. Prof. Lineu Prestes, 2242, São Paulo, SP 05508-000, Brazil
[c] University of São Paulo, São Carlos Institute of Chemistry, Av. Trabalhador São-Carlense, 400, São Carlos, SP 13560-970, Brazil

ARTICLE INFO

Keywords:
LaNi-Zn perovskite
Oxygen mobility
Ni-Zn alloy
Oxygen species
Carbon resistance

ABSTRACT

Carbon formation is one of the major problems in methane reforming reactions, mainly in dry reforming of methane (DRM), limiting its industrial competitiveness. Thus, in this work, we investigate the oxygen mobility and carbon resistance of the LaNi-Zn perovskite in the DRM reaction. The catalysts $LaNiO_3$ (LN) and $LaNi_{0.5}Zn_{0.5}O_{3-\delta}$ (LNZn) were synthesized and characterized by XRD, H_2-TPR, CH_4-TPSR-MS, H_2-TPHR-MS, XPS, TGA, Raman, HRTEM, and *quasi-in-situ* DRIFTS-MS, aiming to understand the role of the promoter in coke suppression. The CH_4-TPSR-MS, H_2-TPHR-MS, and Raman analyses revealed that the Zn-substituted catalyst exhibited higher oxygen mobility compared to the LN catalyst, attributed to the oxophilicity of Zn^{2+}, which facilitates carbon gasification. XPS and HRTEM analyses of reduced samples confirmed the presence of metallic Zn^0 on the surface as Ni-Zn alloying. 30 h of TOS showed higher activity for the LN catalyst than the LNZn. However, post-reaction analysis indicated that the addition of Zn increased carbon resistance by 5 times. The formation of the Ni-Zn alloying effectively prevented the removal of Ni particles from the support and their encapsulation by carbon nanotubes. *Quasi-in-situ* DRIFTS-MS has revealed that the LNZn catalyst promotes the formation of intermediate species responsible for carbon oxidation (CH_xO, $HCOO^-$, and HCO_3^-), clearing the anti-carbon behavior of the Zn-substituted catalyst.

1. Introduction

Understanding the carbon formation on catalysts is an important topic of discussion in methane reforming reactions, specifically in dry reforming of methane (DRM). The DRM is an outstanding reaction to mitigate carbon dioxide (CO_2) and methane (CH_4) into syngas, a mixture of H_2 and CO (Eq. 1), which can be used to synthesize high-valued chemicals [1–3].

$$CH_4 + CO_2 \rightarrow 2H_2 + 2CO \quad \Delta H_{298K} = 247\ kJ/mol \tag{1}$$

Due to the highly endothermic nature of the DRM reaction and the high activation energy of both CH_4 (435 kJ mol^{-1}) and CO_2 (526 kJ mol^{-1}), temperatures above 600 °C are required to reach thermodynamic equilibrium during the reaction [4,5]. According to the stoichiometric factor, the CO_2 and CH_4 conversions should be similar, and the H_2/CO ratio is expected to be close to one. However, side reactions, such as the reverse water-gas shift (RWGS) (Eq. 2), led to an H_2/CO ratio lower than 1 due to the partial consumption of H_2 [3,6–9].

$$CO_2 + H_2 \rightarrow CO + H_2O \quad \Delta H_{298K} = 41\ kJ/mol \tag{2}$$

Generally, the major problem of dry reforming is the unavoidable deactivation of the catalyst due to sintering and carbon formation [3,10,11]. Sintering is a prevalent issue in the DRM due to the high operational temperatures, which directly influence carbon formation by accelerating carbon deposition [12]. In fact, among methane reforming processes, DRM is particularly susceptible to carbon formation because of its low hydrogen-to-carbon (H/C) and oxygen-to-carbon (O/C) ratios [8,10].

Catalyst deactivation by carbon can occur due to the encapsulation of active metal sites, pore blockage, filament breakage, or clogging, hindering the contact between the reactant gases and the surface of the catalyst or by increasing the pressure drop in the catalyst bed [12]. At high temperatures (>500 °C), carbon formation is formed primarily

* Corresponding authors.
E-mail addresses: jubertoldi@usp.br (J. Bertoldi), mschmal@usp.br (M. Schmal).

https://doi.org/10.1016/j.apcata.2025.120400
Received 13 April 2025; Received in revised form 29 May 2025; Accepted 3 June 2025
Available online 8 June 2025

through CH_4 cracking (Eq. 3), while lower temperatures (<500 °C) lead to carbon formation by the reverse Boudouard reaction (Eq. 4) [13].

$$CH_4 \rightarrow C + 2H_2 \ \Delta H_{298} = 75 \text{ kJ/mol} \quad (3)$$

$$C + CO_2 \rightarrow 2CO \ \Delta H_{298} = 172 \text{ kJ/mol} \quad (4)$$

In reforming reactions, carbon is typically present in three distinct forms: C_α, C_β, and C_γ, which are classified based on their reactivity with hydrogen at specific temperature ranges: 150–220 °C, 530–600 °C, and > 650 °C, respectively [3,10,12,14,15]. C_α is a highly active carbon species generated through the cracking of CH_4 at the metal site (Eq. 1). These species are reported as a non-deactivating carbon form that acts as a reaction intermediate, contributing primarily to CO formation, as C_α (adsorbed on the active site) reacts with adsorbed oxygen species [12, 15]. C_α species that do not undergo oxidation due to the absence of adjacent oxygen species at the metal site are transformed into C_β, a less-activity carbon species responsible for the formation of a polymeric amorphous film on the metal surface that serves as a precursor for nanotubes [15]. Subsequently, C_β can migrate from the metal site to the support, forming the graphitic C_γ carbon type, the most deactivating form of carbon [12,15,16].

Therefore, carbon deposition is a result of the balance between the formation and gasification of carbon, which depends on the active site, support, the interaction between both, the mechanism of reaction, and temperature, becoming a challenge to the DRM process [16,17].

Nickel-supported catalysts are the most widely used systems in methane reforming reactions due to their ability to activate CH_4 and their low cost [1,18,19]. However, their major limitations include deactivation by sintering due to the high temperatures and carbon deposition caused by the slower carbon gasification on the nickel surface compared to its formation rate [16]. In this regard, perovskite-type oxides $LaNiO_3$ (ABO_3) have been studied as an alternative material for stabilizing the nickel structure in metal-oxide systems by means of a stronger metal-support interaction than supported catalysts [20]. In this structure, site A can accommodate rare-earth, alkaline, and alkaline-earth metals, while the B site is usually a transition metal responsible for the catalytic activity [20,21].

The ABO_3 structures can be decomposed in highly dispersed Ni^0/La_2O_3 through *in-situ* activation, thus improving the catalytic performance and stability [20,22,23]. Therefore, these complex oxides can be modified by partial substitutions on both A and B sites, resulting in an $A_{1-x}A'_xB_{1-x}B'_xO_3$ structure. This structure favors the appearance of structural defects, such as oxygen vacancies, which can lead to higher oxygen mobility and, therefore, improve the ability of the catalyst in oxidizing carbon [24,25].

There are several reported cases of partial substitution by introducing other metals on site B, forming an $AB_{1-x}B'_xO_3$ perovskite-type structure [26–31]. However, if the incorporation degree is 50 % and the B′ and B cations have different sizes and charges, a new arrangement in the structure can occur, giving rise to double perovskites-type, like $A_2BB'O_{6-\delta}$ or $AB_{0.5}B'_{0.5}O_{3-\delta}$ [32]. These complex rearrangements may promote an interesting phenomenon, *i.e.*, a synergetic effect caused by the interaction between B and B′ metal with different oxidation states.

In this context, limited studies have explored the incorporation of Zn as a substitute for Ni in perovskite structures at a 50 % substitution level. This limitation occurs due to the charge disparity between Ni and Zn, which makes neutralizing the ABO_3 framework difficult. However, their similar ionic radii facilitate the formation of oxygen vacancies, significantly enhancing carbon oxidation and improving catalyst stability and performance [33–35].

Moradi et al. [36] investigated the partial substitution of Ni by Zn during the DRM and found that Zn stabilizes the Ni^0 particles on the surface, inhibiting sintering by means of strong interactions caused by Zn-La-O bonds. Velisoju et al. [37] found that a synergetic effect occurs between Zn and Ni, leading to the formation of a Ni-Zn alloy, which increases oxygen vacancies, the resistance to carbon formation, and stabilizes nickel metallic particles. Chatla et al. [38] demonstrated that the addition of Zn increases the metal-support interaction, stabilizes Ni particles, and prevents the formation of carbon through the formation of NiZn alloy.

In this study, we investigated the incorporation of Zn into the Ni site within the perovskite structure $AB_{1-x}B'_xO_{3-\delta}$ and its impact on enhancing oxygen mobility, catalytic performance and stability in the dry reforming of methane. A comprehensive set of characterizations were conducted to elucidate perovskite formation, oxygen mobility enhancement, and the mechanisms of carbon deposition and removal on the LNZn catalyst compared to the undoped catalyst.

2. Experimental section

2.1. Chemicals and supplies

Nickel nitrate ($Ni(NO_3)_2.6H_2O$ – 97 %), citric acid (99.5 %), and ethylene glycol (99 %) were purchased from Sigma Aldrich. Lanthanum nitrate ($La(NO_3)_3.6H_2O$ – 99,9 %) and zinc nitrate ($Zn(NO_3)_2.6H_2O$ – 96 %) were obtained from Thermo Scientific Chemicals and Synth, respectively. All the chemicals were analytical grade and used without further purification. High-purity commercial CH_4 (99.995 %) and CO_2 (99.99 %) came from White Martins, and N_2 (99.999 %) was purchased from Special Gases.

2.2. Synthesis of the catalyst

The $LaNi_{1-x}M_xO_3$ (x = 0 or 0.5; M = Zn) perovskites were synthesized by Polymerization Complex Route (PCR) [24,39]. Aqueous solutions of the metallic precursors $La(NO_3)_3.6H_2O$, $Ni(NO_3)_2.6H_2O$, and ZnO $(NO_3)_2.6H_2O$ were prepared and mixed at room temperature according to the desired molar ratio. Then, 1 mol L^{-1} citric acid (AC) was incorporated into the solution under vigorous stirring to obtain an AC/metals ratio of 1.1. Then, the mixture was heated to 60 °C and kept under stirring for 30 min. Ethylene glycol (EG) was subsequently added at an AC/EG ratio of 1.5, and the temperature was raised to 90 °C, remaining under this condition until the formation of a polymeric resin. The resin was dried overnight at 110 °C and then calcined at two calcination steps. The first step is to calcinate the material at 500 °C for 1 h with a heating rate of 2 °C min^{-1} under synthetic air to eliminate organic compounds. The second step involved the formation of the perovskite structure at a calcination temperature of 750 °C for 4 h under synthetic air (30 mL min^{-1}). The samples were named LN ($LaNiO_3$) and LNZn ($LaNi_{0.5}Zn_{0.5}O_3$).

2.3. Characterization

The crystalline structure of the samples was analyzed by XRD using a Rigaku MiniFlex 300/600 with copper radiation (CuK_α = 1.541862 Å) operating at 30 kV and 10 mA. The diffraction patterns were compared to the Inorganic Crystal Structure Database (ICSD). The specific surface areas and adsorption/desorption isotherms were determined by the BET method using N_2 physisorption at −196 °C on an Anton Paar NOVA800 analyzer. The actual Ni content in the catalyst was determined by ICP-OES using an Agilent 5800 spectrometer. H_2-TPR, CO_2-TPD, CO-pulse chemisorption, and TPO were performed at a Micromeritics AutoChem II 2920 chemisorption analyzer. CH_4-TPSR-MS and H_2-TPSH-MS were recorded using a Micromeritics AutoChem II 2920 and a Pfeiffer Vacuum TSU 065D mass spectrometer. The morphology of the reduced *ex-situ* catalysts at 700 °C and the spent catalysts following DRM at 800 °C was visualized by HRTEM (Jeol JEM-2100) at an accelerating voltage of 200 kV. Raman spectra were taken on a Renishaw inVia spectrometer system with a 532 nm laser using 5 % of the laser power. Thermogravimetric analyses were performed at a Shimadzu DTG-60H in temperatures ranging from room temperature to 1000 °C in the presence of synthetic air. XPS was performed in a Spectra FlexPS on the reduced *ex-*

situ catalyst at 700 °C using Al Lα radiation at 1486.71 eV. DRIFTS-MS spectra were recorded using a Shimadzu IRPrestige-21 spectrometer equipped with a Harrick cell and a Pfeiffer Vacuum OmniStar mass spectrometer. The reduced catalysts were first exposed to a 10 % CH_4/N_2 mixture at room temperature (RT) for 5 min, then purged with N_2. Subsequently, a 10 % CO_2/N_2 mixture was introduced for 5 min and purged with N_2. The temperature was heated to 550 °C (10 °C min^{-1}), and the spectra were collected at temperatures ranging from 150 to 550 °C. Additional details about the experimental procedure can be found in the Supplementary Information.

2.4. DRM performance tests

The $LaNi_{1-x}M_xO_3$ (x = 0 or 0.5; M = Zn) perovskites were evaluated in the Dry Reforming of Methane (DRM). 30 h tests were performed in a fully automated fixed-bed catalytic reactor Microactivity-Effi (PID Eng&Tech®), equipped with a Hastelloy X tubular reactor (9.1 mm diameter) at atmospheric pressure. 25 mg of catalyst, 20 w/w% of silicon carbide (SiC – Sigma-Aldrich, 400 mesh), and a weight hourly space velocity (WHSV) of 120 L g_{cat}^{-1} h^{-1} were used. First, the catalysts were reduced *in situ* under H_2 flow (100 mL min^{-1}) at 700 °C with a heating rate of 10 °C min^{-1}, remaining for 1 h. After the reduction, the temperature was set at 700 °C, 750 °C, and 800 °C, with the feed stream set at CH_4:CO_2:N_2 = 0.5:0.5:1 at atmospheric pressure. The gases were analyzed using a gas chromatographer (Shimadzu - GC2010 Plus) equipped with a thermal conductivity detector (TCD), a flame-ionization detector (FID), and two capillary columns - Carboxen 1010 and SH-Qbond.

The conversion of CO_2 and CH_4, the selectivity to H_2 and CO, and the reaction rates were calculated based on the following equations:

$$Xi\ (\%) = \frac{[F_i]_{in} - [F_i]_{out}}{[F_i]_{in}} \times 100 \quad (5)$$

$$Sj\ (\%) = \frac{[F_j]_{out}}{\sum([F_j]_{out})} \times 100 \quad (6)$$

$$(H_2/CO)_{out} = \frac{[F_{H_2}]_{out}}{[F_{CO}]_{out}} \quad (7)$$

$$-ri\ \ (\text{mmol gNi}^{-1}\ s^{-1}) = \frac{[n_i]_{reacted}}{W_{cat} * 60} \quad (8)$$

Turnover Frequencies (s^{-1}) were calculated from Eq. 9 [40].

$$TOFi\ (s^{-1}) = \frac{[n_i]_{reacted}}{W_{cat} * M_{Ni} * \frac{\text{Ni Dispersion}}{58.7} * 60} \quad (9)$$

X*i* is the CH_4 and CO_2 conversion. S*j* is the product selectivity, $(H_2/CO)^{out}$ is the syngas ratio, n*i* is the mol min^{-1} of CH_4 and CO_2 reacted, W_{cat} is the catalyst weight (g), and M_{Ni} is the Ni loading (wt%). (F_{in}) and (F_{out}) are the gases molar flow in and out of the reactor, respectively. Ni dispersion (%) was calculated based on the CO-pulse chemisorption.

The apparent activation energy (E_a) was estimated by the Arrhenius equation plotting the natural logarithm of TOF (s^{-1}) versus 1000/T, as follows:

$$\ln(TOFi\ \ (s^{-1})) = \ln A - \frac{Ea}{RT}(10) \quad (10)$$

where *R* is the universal gas constant (8.314 J mol^{-1} K^{-1}), and *T* is the absolute temperature in Kelvin (K).

3. Results and discussion

3.1. Characterization

Fig. 1 depicts the XRD patterns of the catalysts LN and LNZn

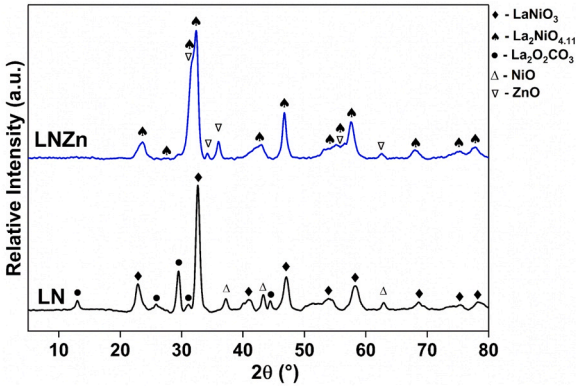

Fig. 1. XRD patterns of the catalysts LN and LNZn.

synthesized by the PCR method. According to the literature, synthesis methods based on citrate complex favor the formation of segregated phases due to exothermic reactions during its decomposition (>400 °C) [24,41]. The LN catalyst exhibited a multi-phase mixture consisting of a perovskite phase and segregated phases. The rhombohedral perovskite $LaNiO_3$ (ICSD Code 034–1181), with space group R-3cH, was confirmed at 2θ = 22.73° (1 0 0), 32.63° (1 1 0), 46.94° (2 0 0), and 58.22° (2 1 1). Additionally, segregated phases of lanthanum oxycarbonate ($La_2O_2CO_3$ – ICSD Code 023–0322) and nickel oxide (NiO – ICSD Code 01–071–1179) were also observed. The formation of oxycarbonated species arises from the high affinity of the La^{3+}–O^{2-} pair site, considered a Lewis acid–Brönsted base pair, with CO_2 from the citrate decomposition [22,42,43]. This interaction is facilitated by the high exothermicity and low energy barrier of CO_2 chemisorption on La_2O_3, leading to the formation of CO_3^- compounds and the segregation of nickel oxide outside the perovskite framework [44]. Zn-substituted catalyst (LNZn) exhibited phases corresponding to zinc oxide (ZnO – ICSD Code 01–080–0074, hexagonal), and the orthorhombic spinel perovskite phase, $La_2NiO_{4.11}$ (ICSD Code 01–081–1961), also known as the Ruddlesden-Popper (RP) structure. These results indicate that the partial substitution of Ni used in this work (x = 0.5) exceeds the solubility of Zn in the $LaNiO_3$ structure (x > 0.2), leading to the segregation of single oxides [45]. The formation of the RP phase is attributed to the partial introduction of Zn^{2+} into the $LaNiO_3$ structure, resulting in an imbalance in the oxidation states of Ni and the formation of an oxygen-excess (+δ) perovskite, in this case, $La_2NiO_{4+\delta}$ phase, where a mixture of Ni^{2+} and Ni^{3+} coexist. According to Minervini et al. [46] and Woolley et al. [47], the charge-compensating mechanism on this type of material is related to the oxidation states of nickel, resulting in different averages of the oxidation states, in agreement with the results obtained. In fact, the main diffraction peaks of $La_2NiO_{4.11}$ are obtained at 2θ = 31.37° and 32.54°. In this work, these reflections merge to form a single peak centered at 32.37° with a shoulder at 31.62°. As previously reported by Ponce et al. [48] and Shao et al. [45] in a similar work with substituted perovskites, the merge of peaks is due to the change of the cell parameters of the perovskite structure when the substitution of $Ni^{2+,3+}$ by Zn^{2+} takes place.

The textural properties of the catalysts are displayed in Table 1 and Fig. S1. Both catalysts presented surface area characteristics of perovskite-type oxides calcinated at higher temperatures (<10 g). The

Table 1
Textural and superficial parameters of the fresh catalysts.

Sample	BET surface area (m^2/g)[a]	Average pore diameter[a] (nm)	Pore volume[a] (cm^3/g)
LN	< 10	30	0.05
LNZn	< 10	30	0.02

[a] Determined from N_2 physisorption at −196 °C.

N_2 physisorption isotherms (Fig. S1) exhibited type IV characteristic behavior given by mesoporous (pores between 2 nm and 50 nm) and an H3 hysteresis, indicating a non-homogenous pores distribution [49].

Fig. S2 presents the reduction profile of the LN and LNZn catalysts. Reduction peaks observed within the temperature range of 330 °C in LN are associated with the partial reduction of Ni^{3+} to Ni^{2+} through the formation of intermediary phases [50–53], as described below.

$$4LaNiO_3 + 2H_2 \rightarrow La_4Ni_3O_{10} + Ni^0 + 2H_2O \quad (11)$$

$$2LaNiO_3 + H_2 \rightarrow La_2Ni_2O_5 + H_2O \quad (12)$$

Hydrogen consumption observed at 365 °C and 430 °C for LNZn and LN, respectively, corresponds to the reduction of NiO to Ni^0, indicating weaker interaction of NiO with the perovskite phase [54]. At 580 °C, the LN catalyst exhibits a reduction step associated with the final perovskite reduction, from Ni^{2+} to Ni^0 [50], followed by hydrogen consumption at 650 °C which can be associated with the presence of $La_2O_2CO_3$ on this material, as confirmed by XRD results [51], or even the reduction of intermediate spinel phases which decomposes at this temperature range [52,53].

In the case of the LNZn catalyst, where the spinel phase $La_2NiO_{4.11}$ is observed, the final reduction peak occurs at higher temperatures (640 °C), which is attributed to the reduction of Ni^{2+} on the RP phase to Ni^0, indicating that the introduction of Zn^{2+} leads to a higher metal-support interaction [52]. The stronger metal-support interaction on the Zn-substituted catalyst could be explained by the formation of Ni-Zn alloy due to the similar ionic radii between these two metals, leading to the stabilization of Ni metallic particles and increasing oxygen vacancies [37]. The formation of the metallic alloy justifies the occurrence of a peak at 720 °C on this material, which is not verified in the LN catalyst, indicating that a part of Zn^{2+} is reduced [37]. According to Velisoju et al. [37], the reduction of Zn^{2+} to Zn^0 starts at 650 °C, and the formation of the metallic alloy occurs at temperatures above 700 °C, in agreement with the H_2-TPR results in this work.

The basic sites were quantitatively evaluated using CO_2-TPD. As demonstrated in Fig. S3 and Table 2, there are three types of basic sites identified on the CO_2 desorption temperature profiles: weak (<200 °C), moderate (200 °C-550 °C), and strong (>550 °C). Weak basic sites are associated with bicarbonate species, which are not effectively involved in DRM [54]. Bidentate and monodentate carbonates desorb sequentially at temperatures ranging from 200 to 550 °C, corresponding to the medium-strength basic sites [55]. Strong basic sites are characterized by CO_2 desorption at temperatures above 550 °C and are attributed to the formation of oxycarbonate species ($La_2O_2CO_3$) on the La_2O_3 matrix support [49,54,55].

As indicated by Table 2, the total amount of basic sites follows the order of LN > LNZn. Similar quantities of weak basic sites were obtained for both catalysts. In contrast, there is a significant difference in the medium-strength basic sites for Zn-containing catalyst, indicating that the introduction of Zn does not favor the formation of bidentate and monodentate carbonates.

As illustrated in Fig. S3, LN catalysts exhibited a higher amount of strong basic sites (0.220 mmol CO_2 g_{cat}^{-1}) with a desorption peak at 750 °C, followed by LNZn (0.100 mmol CO_2 g_{cat}^{-1}) with a desorption peak at 800 °C. However, this behavior suggests that the LNZn catalyst induces a stronger interaction with CO_2, as indicated by the higher desorption temperature. According to Ewald and Hinrichsen [55], at higher temperatures, CO_2 dissociates on the surface of Ni, producing gaseous CO and oxygen, which remains on the Ni surface and can react with carbon deposits during DRM.

Table 2
CO_2-TPD of the catalysts reduced at 700 °C.

Sample	Basic sites (mmol CO_2 g_{cat}^{-1})*			
	Weak (<200 °C)	Medium (250–550 °C)	Strong (>550 °C)	Total
LN	0.020	0.045	0.220	0.285
LNZn	0.010	0.022	0.100	0.132

* CO_2 desorption was calculated based on the integration of the peaks and a calibration curve.

CH_4-temperature programmed surface reaction (CH_4-TPSR) was performed in the absence of CO_2 to investigate the activation of CH_4 and the effect of carbon deposits (Fig. 2 A-C). Fig. 2 A and Table S1 show the methane consumption profile curve and temperatures for the initiation and inhibition of methane cracking. According to the results, all catalysts present methane activation at an initial temperature of methane cracking following the order: LN (405 °C) < LNZn (520 °C), thus indicating that methane cracking is facilitated on the non-substituted catalyst.

On the other hand, the lower inhibition temperature for LN (590 °C) indicates that carbon deposits originated from the methane cracking (Eq.3) block the nickel sites quicker than the LNZn catalyst. In the case of Zn-substituted catalysts, the methane cracking declines at 712 °C, which indicates that the introduction of Zn has a positive effect on carbon deposition on the surface of the catalyst. Additionally, the LNZn catalyst shows a peak after the inhibition point (840 °C), possibly associated with the formation of new metallic active sites [56,57], as described by Eqs.13 and 14.

$$NiO + C_{(s)} \rightarrow CO + Ni^0 \quad (13)$$

$$2NiO + C_{(s)} \rightarrow CO_2 + 2Ni^0 \quad (14)$$

The evolution of H_2 and other molecules was monitored using a mass spectrometer during CH_4-TPSR. Fig. 2B-C depict the recorded signals of H_2, H_2O, CO, CO_2, and O_2 throughout the process. The consumption of CH_4 closely correlates with the evolution of H_2, indicating that CH_4 bond cleavage occurs at the nickel site via methane decomposition (Eq. 3). Furthermore, the evolution of H_2O, CO, CO_2, and O_2 is observed throughout the CH_4-TPSR, suggesting that the carbon formed from CH_4 dissociation, along with a portion of the released hydrogen, reacts with adsorbed oxygen species [58,59].

No evident evolution of oxygen species is observed for the LN catalysts (Fig. 2B). In contrast, the LNZn catalyst (Fig. 2 C) exhibited the evolution of oxygen species varying with the increase in temperature, with a maximum oxygen evolution at the inhibition point, indicating that the partial substitution of Ni by Zn enhances the oxygen mobility on the perovskite [33–35]. Additionally, the spectrum of the LNZn catalyst provides evidence for the formation of new metallic sites at 840 °C, as suggested above, attributed to the increasing evolution of CO (Eq.13) and H_2O, as described by the Eq. 15:

$$Perovskite - NiO + H_2 \rightarrow H_2O + Ni^0 \quad (15)$$

Aiming to investigate the type of carbon formed, the H_2-temperature hydrogenation reaction (H_2-TPHR) coupled with a mass spectrometer (Fig. 2D-F) and Raman spectroscopy were performed after CH_4-TPSR. The ion fragments monitored during the H_2-TPHR were CH_3^+, and CH_4^+, H_2O^+, CO^+, O_2^+ and CO_2^+ (Fig. 2E-F).

Based on the results of the H_2-TPHR, the LN catalyst exhibited two peaks: one within the range of 140 °C and a broader peak centered at 615 °C. Mass spectroscopy data for the LN catalyst (Fig. 2E) revealed the formation of H_2O, CO_2, and CH_4 at 140 °C, indicating the removal of carbide Cα, a highly reactive carbon species [60]. Furthermore, the formation of H_2O and CO_2 is ascribed to the reaction of both H_2 and C with oxygen species from the sub-surface of the catalyst. Mass spectrum data also identified a peak related to the evolution of H_2O at 325 °C, which was not verified in the H_2-TPHR signal (Fig. 2D). At 615 °C, only methane ion fragments evolved, without the concurrent formation of CO, CO_2, or H_2O, indicating the presence of graphitic carbon (Cγ), a less active species than other types of carbon [60]. Therefore, these findings imply that the bulk oxygen species probably do not have a substantial contribution to carbon removal on the LN catalyst at elevated

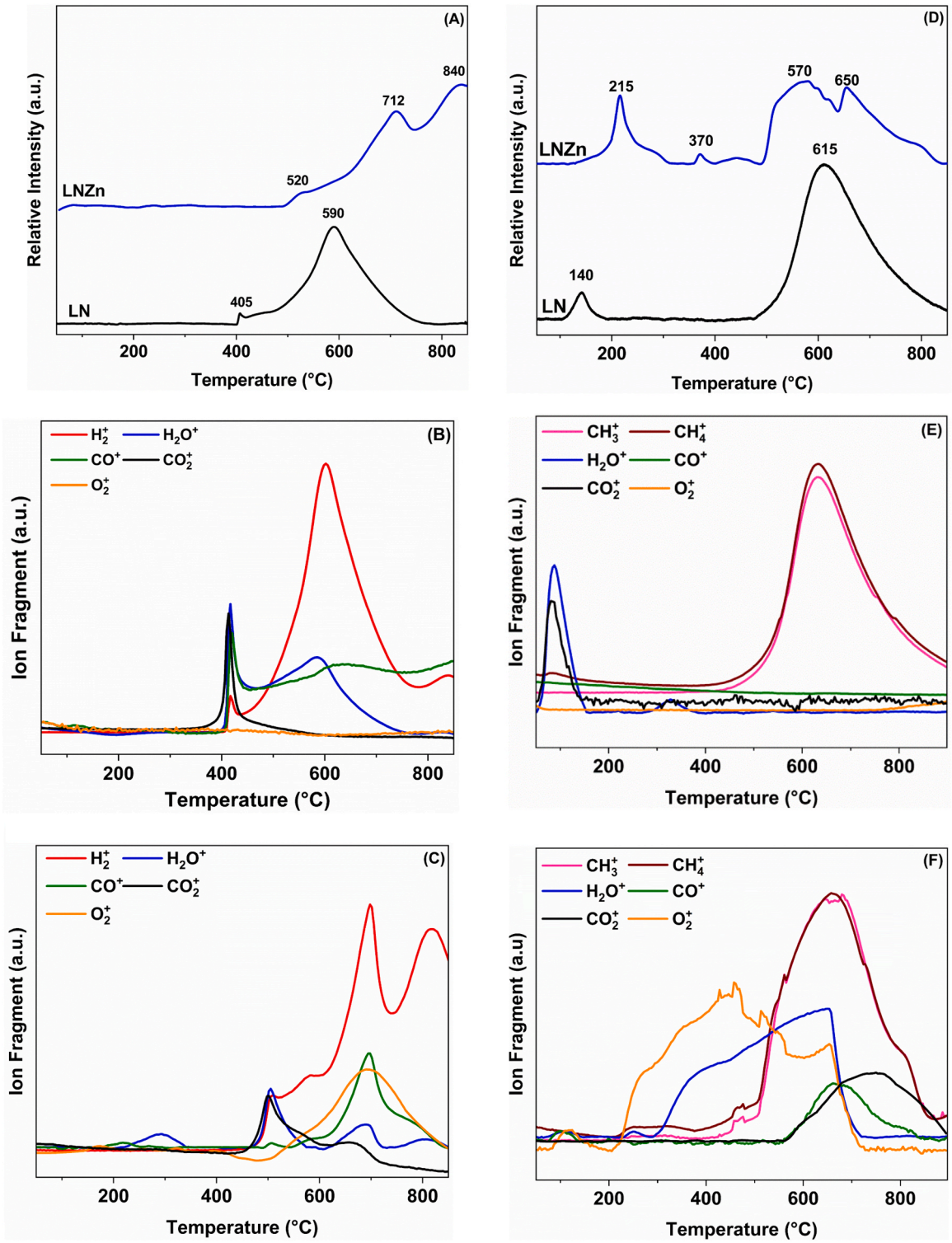

Fig. 2. (A) CH_4-TPSR performed under 25 %CH_4/75 % He, total flow of 50 mL and 25 mg of the catalysts. (B) and (C) MS ion fragments monitored during CH_4-TPSR. (D) H_2-TPHR performed after the CH_4-TPSR. (E) and (F) MS ion fragments monitored during H_2-TPHR.

temperatures.

The hydrogenation profiles of the LNZn catalyst reveal three distinct temperature regions: first at 215 °C, second at 370 °C, and third region above 500 °C. In contrast to the H_2-TPHR results, where no peaks were obtained at temperatures below 150 °C, the mass spectroscopy data of LNZn (Fig. 1 F) indicated the release of H_2O, O_2, and CO at this temperature range, demonstrating that, at low temperatures, both H_2 and carbon species preferentially interact with bulk oxygen species, rather than forming methane, as also verified by Xu et al. [61].

In the first region evidenced by a peak in H_2-TPHR at 215 °C, the LNZn catalyst exhibits the coexistence of H_2O and O_2 evolution, along with CH_4 formation, indicating that the partial substitution of Ni by Zn enhances oxygen species mobility due to the higher oxophilicity of Zn and the formation of oxygen vacancies by doping the Ni-site [38,62], as evidenced by the formation of oxygen-containing species. The Zn-substituted catalyst presented a broader peak range related to the

evolution of O_2 and H_2O at 460 °C and 650 °C, respectively, with both species coexisting up to 700 °C. At this point, the H_2O formation declines, corresponding to the cessation of O_2 evolution, and the preferred formation of other compounds becomes more prominent.

The third temperature region of hydrogenation (>600 °C) is associated with methane formation, indicating the presence of graphitic carbon (Cγ) [60], as identified in the LN catalyst. However, the shoulder observed at 570 °C in the LNZn catalyst is related to the evolution of O_2 and H_2O, as discussed above and observed by mass spectroscopy (Fig. 2 F). In addition to methane formation, the LNZn catalyst produced CO and CO_2 above 700 °C, due to the consumption of adsorbed oxygen species. The formation of H_2O, CO, and CO_2 demonstrates higher oxygen

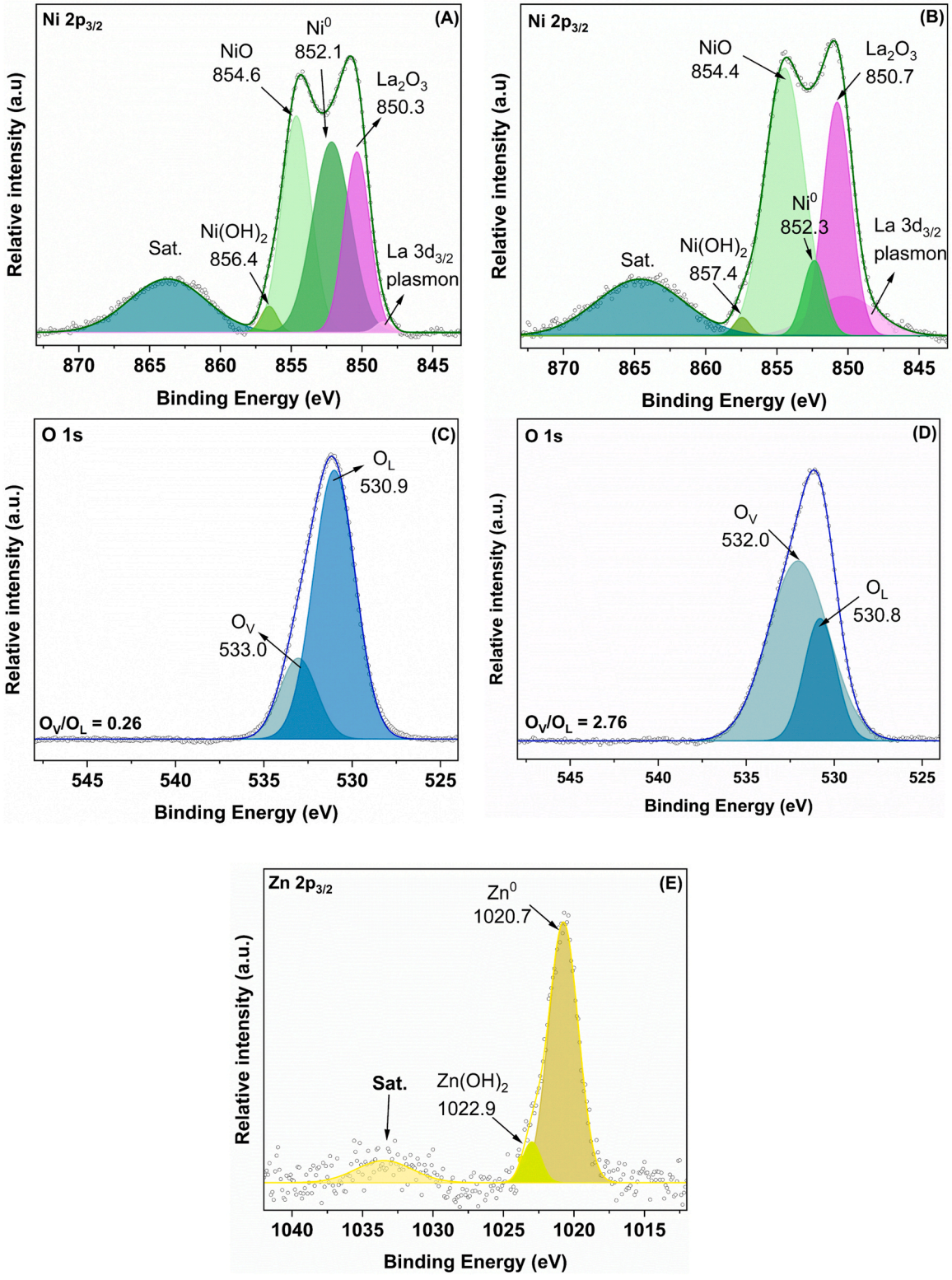

Fig. 3. XPS measurements performed on LN and LNZn after H_2 reduction at 700 °C, simulating an in-situ reduction prior to DRM reaction. Ni 2p3/2 region of LN (A) and LNZn (B); O 1s region of LN (C) and LNZn (D); Zn 2p3/2 region of LNZn (E).

mobility to the LNZN catalyst compared to the LN catalyst, with different oxygen atoms reacting with H_2 and carbon deposits, resulting in oxygen-containing species and vacancies [61].

The Raman spectra obtained after CH_4-TPSR-MS (Fig. S3) revealed the characteristic carbon bands D (1348 cm^{-1}), G (1580 cm^{-1}), and 2D (2680 cm^{-1}) on the LN catalyst, but not such bands were observed on the LNZn spent catalyst [37,58,63,64]. The degree of graphitization (I_D/I_G) was 1.29 for LN, while it was negligible for LNZn. These results confirm the primary form of carbon generated during CH_4-TPSR-MS as graphite-like, in agreement with the H_2-TPHR results.

XPS measurements were performed on LN and LNZn catalysts after H_2 reduction at 700 °C, simulating an *in-situ* reduction prior to the DRM reaction. The results of the analysis are presented in Fig. 3 and Fig. S5. The characterization of La-Ni-based perovskites by XPS turns out to be quite difficult due to the overlapping binding energies of La $3d_{3/2}$ and Ni $2p_{3/2}$ (845–860 eV). As a result, Ni $2p_{3/2}$ cannot be analyzed independently without indexing La $3d_{3/2}$ components.

The La 3d spectrum of LN and LNZn (Fig. S5C-D) shows the characteristic La 3d core split into La $3d_{5/2}$ and La $3d_{3/2}$. Both catalysts exhibit an identical La $3d_{5/2}$ region with four components corresponding to two lanthanum species: La_2O_3 (833 eV), $La(OH)_3$ (835 eV), and their respective satellite peaks at 837 eV, and 839 eV [65,66]. The satellite separation (ΔE_{sat}) for La_2O_3 and $La(OH)_3$ were found to be 3.7 eV and 4.2 eV, respectively, which agrees with the literature for similar materials [66]. The La $3d_{3/2}$ region presents a peak for La_2O_3 at 850.7 eV, and its satellite peak is observed between 853.9 and 854.1 eV.

The presence of $La(OH)_3$ is attributed to the high reactivity of La_2O_3 with air moisture during the transport of the sample from the reactor, where the catalysts were reduced, to the XPS analysis chamber, or the direct reduction of La_2O_3 to $La(OH)_3$ after reduction [67,68]. In contrast, La_2O_3 is associated with the decomposition of the perovskite structure ($LaNiO_3$/$La_2NiO_{4.11}$) into La_2O_3 and metallic Ni.

The Ni $2p_{3/2}$ region of LN and LNZn reduced at 700 °C is depicted in Fig. 3A-B. As expected, the overlapping in this region resulted in a peak corresponding to La_2O_3 at 850.7 eV, along with a plasmon loss feature of La $3d_{3/2}$ between 850.1 and 848.3 eV [65,66]. The Ni components in the Ni $2p_{3/2}$ region indicate the presence of metallic Ni particles in the binding energy of 852 eV, NiO at 854 eV, $Ni(OH)_2$ between 856 and 857 eV, and a satellite peak of NiO at 865 eV [37,65,66]. Additionally, the presence of NiO can partly be attributed to the partial oxidation of metallic Ni, as surface Ni readily oxidizes upon exposure to air [37].

Based on the deconvolution of Ni 2p spectrum, the amount of metallic Ni on the surface was estimated as the ratio $Ni^0/(Ni^0 + Ni^{2+} + Ni^{2+}_{hydro})$. For the LN catalyst, the ratio of metallic Ni was found to be 0.51, whereas for LNZn, the metallic Ni on the surface corresponds to 0.13. These results indicate that, as demonstrated by H_2-TPR, the introduction of Zn^{2+} promotes a stronger interaction with Ni, which makes its reducibility difficult.

A single peak is observed in the O 1 s region (Fig. 3C-D), which can be deconvoluted into two distinct oxygen species located at 530.8 eV and 532–533 eV. The lower binding energy peak corresponds to lattice oxygen species (O_L), while the higher binding energy peak is attributed to oxygen vacancies on the surface (O_V) [37]. The O_V/O_L ratio provides valuable insights into oxygen mobility and reactivity [37]. The LN catalyst shows an O_V/O_L ratio of 0.26, while LNZn shows an increase to 2.26, which indicates higher oxygen mobility, in agreement with the results obtained by CH_4-TPSR and H_2-TPHR, where oxygen evolution and oxygen-containing species are verified. According to Velisoju et al. [37], these observations are related to the surface migration of Zn from the support to form an alloy with Ni. This hypothesis is supported by the Zn $2p_{3/2}$ spectrum (Fig. 3E), revealing the presence of metallic Zn on the surface of the catalyst after reduction, with a peak at 1020.7 eV, as also demonstrated by Chatla et al. [38]. Based on the deconvolution of the peak, 91 % of the Zn on the surface exists as Zn^0.

3.2. Catalytic results

The activity and stability of the LN and LNZn catalysts were evaluated in the dry reforming of methane (DRM) for 30 h at 700 °C, 750 °C, and 800 °C, with a CH_4:CO_2:Ar: ratio of 0.5:0.5:1, and WHSV = 120 L g_{cat}^{-1} h^{-1}. Fig. 4 displays the conversions and H_2/CO ratios of the LN and LNZn catalysts for different temperatures over 30 h of TOS.

The LN catalyst presented higher conversions of CH_4 and CO_2 and H_2/CO ratio for all temperatures than LNZn catalyst, as shown in Fig. 4 A, suggesting that the nickel content on the LN catalyst influences significantly catalytic activity. For the LN catalyst, the initial conversions of CH_4 were 68 %, 90 %, and 97 % at 700 °C, 750 °C and 800 °C, respectively. Noteworthy is the high stability observed at 800 °C. However, at 750 °C, a deactivation tendency is observed, possibly associated with the blockage of nickel sites due to carbon deposition. At 700 °C, the LN catalyst reached a steady state condition after 5 h.

The CO_2 conversions are displayed in Fig. 4B. At 800 °C, the conversion reached 89 %, remaining stable over the 30 h of reaction. The conversion decreased at 750 °C after 17 h, from 84 % to 81 %, and at 700 °C, CO_2 conversion increased from 65 % to 72 % after 5 h. The H_2/CO ratio shows a gradual increase with the temperature, following the order: 0.76 (700 °C) < 0.85 (750 °C) < 0.96 (800 °C).

CH_4 conversions of the LNZn catalyst were observed to be between 44 % and 47 % across 30 h of TOS. At 700 °C, the conversion increased from 43 % to 50 % after 5 h. At 750 °C, the conversion stabilized at 45 %. At 800 °C, the CH_4 conversion was 50 % up to 15 h and then decreased but increased again after 5 h. It suggests that the nickel sites are blocked by carbon deposition and subsequently were auto-regenerated, probably through the remotion of carbon (releasing CO_2) and the formation of new Ni metallic sites, as observed in the CH_4-TPSR-MS analyses (Fig. 2). According to the literature [37,38,45], the Ni-Zn oxides can undergo the formation of a Ni-Zn alloy upon reduction, as confirmed by XPS analysis (Fig. 3) of the reduced catalyst. This alloy formation creates a strong interaction between Ni and Zn, which hinders the metallic Ni^0 formation at the surface and may explain the lower CH_4 conversion compared to the LN catalyst.

For the LNZn catalyst, CO_2 conversion was 65 % at 750 °C and 800 °C, whereas at 700 °C, the conversion rate dropped to 63 % after 10 h, remaining stable thereafter. The H_2/CO ratio follows: 0.71 (700 °C) > 0.67 (750 °C) > 0.65 (800 °C). These values are significantly lower than the LN catalyst, suggesting the occurrence of side reactions in the presence of Zn. The formation of the Ni-Zn alloy and the high surface concentration of Zn on the reduced catalyst enhances the adsorption strength of reactive oxygen and intermediate species due to the higher oxophilicity of Zn compared to Ni [62], as evidenced by CH_4-TPSR, and H_2-TPHR. These adsorbed species preferentially bind to Zn atoms, leading to a transition of Zn to a partially oxidized $Zn^{\delta+}$ state during the DRM reaction [62], which creates oxygen vacancies and can improve the oxidation of coke deposits through reactions with the oxygen species coming from the inlet gases, leading to higher formation of CO [33,34,37,69,70].

Fig. 5 and Table 2 summarize the catalytic activity, the reaction rate, and the turnover frequency (TOF) of the catalysts LN and LNZ at 700 °C, 750 °C, and 800 °C over 30 h of TOS. The CH_4 and CO_2 reaction rates for the LN catalyst increased from 0.27 to 0.31 and 0.34 and from 0.25 to 0.28 and 0.30 mmol g_{cat}^{-1} s^{-1}, respectively, as the temperature increased. The corresponding CH_4 and CO_2 TOF followed the same behavior, increasing from 0.86 to 0.99 and 1.1, and from 0.80 to 0.88 and 0.93 s^{-1} as the temperature increased from 700 to 750, and 800 °C. These results agree very well with literature TOF results from $LaNiO_3$-derived catalysts [65].

For the LNZn catalyst, it was observed that the reaction rate of CH_4 and CO_2 increased with an increase in temperature from 750 °C to 800 °C, 0.21–0.22, and 0.22, to 0.26 mmol g_{cat}^{-1} s^{-1}, respectively. It is interesting to notice that, at 700 °C, the reaction rate from both CH_4 and CO_2 is higher than at 750 °C and 800°C, 0.25 and 0.23, respectively,

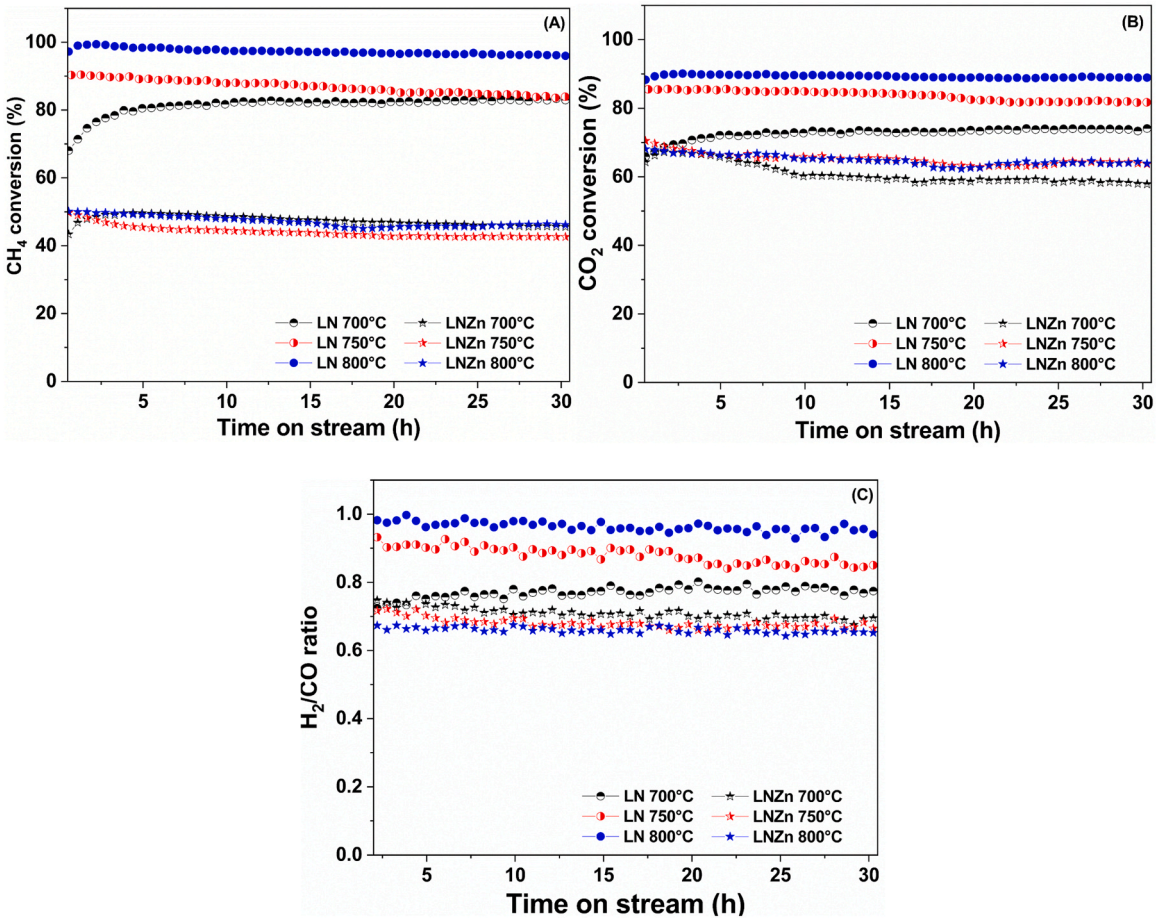

Fig. 4. 30 h stability test of the LN and LNZn catalysts under DRM condition. A) CH_4 conversion, B) CO_2 conversion, C) H_2/CO ratio. Reaction conditions: atmospheric pressure, T = 700, 750, and 800 °C, CH_4:CO_2:Ar: 0.5:0.5:1. WHSV= 120 L $g_{cat}^{-1}h^{-1}$.

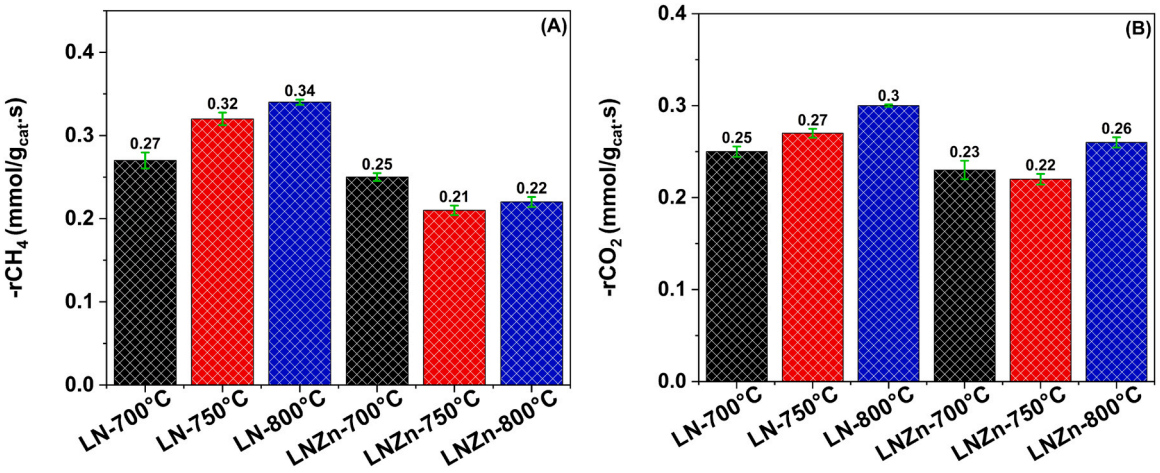

Fig. 5. CH_4 and CO_2 reaction rate of the LN and LNZn catalyst in different temperatures over 30 h of TOS.

suggesting that, at a higher temperature than 700°C, the surface of the catalyst is saturated by intermediate species. The TOF follows the same trend: TOF CH_4 starts at 2.68 s^{-1} at 700 °C, decreases to 2.23 s^{-1} at 750 °C, and then increases to 2.40 s^{-1} at 800 °C. Meanwhile, TOF CO_2 is measured in 2.40 s^{-1} at 700 °C, 2.35 s^{-1} at 750 °C, and 2.77 s^{-1} at 800 °C. These results indicate that, despite lower overall CH_4 and CO_2 conversion than the LN catalyst, the LNZn catalyst exhibits at least twice the efficiency in converting reactant molecules per active site. Table 3

As observed in Table 4, the performance of the synthesized catalysts in this work is comparable to the TOF values reported in the literature for Ni-based systems. Notably, the LNZn catalyst exhibited superior overall TOF values, increasing about 2 times at 700 and 800 °C when compared to the LN catalyst, highlighting the beneficial effect of Zn incorporation.

To understand the effect of Zn introduction in the perovskite lattice in terms of CH_4 and CO_2 activation, the apparent activation energies (E_a)

Table 3
CH_4 and CO_2 conversions, reaction rate, and TOF of DRM different temperatures.

Catalyst	T (°C)	xCH_4 (%)[a]	xCO_2 (%)[a]	$-rCH_4$(mmol g_{cat}^{-1} s^{-1})[a]	TOF CH_4 (s^{-1})[a]	$-rCO_2$(mmol g_{cat}^{-1} s^{-1})[a]	TOF CO_2 (s^{-1})[a]
LN	800	97	89	0.34	1.1	0.30	0.93
	750	87	83	0.32	0.99	0.28	0.88
	700	81	72	0.27	0.86	0.25	0.80
LNZn	800	47	64	0.22	2.40	0.26	2.77
	750	44	65	0.21	2.23	0.22	2.35
	700	47	60	0.25	2.68	0.23	2.40

[a] Average conversion, reaction rate, and TOF over 30 h of TOS.

Table 4
Reported TOF values for CH_4 in DRM over various Ni-based catalysts from the literature.

Catalyst	T (°C)	TOF CH_4 (s^{-1})	Reference
15 wt% Ni–15Ce–20Al	850	0.31	[71]
12 wt% Ni/α-Al_2O_3	850	0.10	[71]
Ni−1Ce-Al	800	1.15	[72]
7 wt%Ni/Al_2O_3	700	0.71	[73]
15 wt% Ni/7La-Si	700	0.66	[74]
15 wt% Ni–15Fe–20Al	600	0.04	[75]
$LaNiO_3$	550	0.87	[65]
LN	800	1.10	This work
LN	700	0.86	This work
LNZn	800	2.40	This work
LNZn	700	2.68	This work

of the catalysts LN and LNZn were calculated based on the Arrhenius equation. The results obtained are presented in Fig. 6. As reported in the literature, the apparent activation energies (E_a) for CH_4 in Ni-based catalysts for DRM ranges from 29.3 to 360 kJ mol^{-1}, while the E_a for the CO_2 are reported to be 30.1 kJ mol^{-1} to 137 kJ mol^{-1}, depending on several aspects, such as the nature of the support, promoters, and reaction conditions [76–79].

For CH_4 and CO_2 activation, the LNZn catalyst presented the lower activation energies, 22.18 kJ mol^{-1} and 14.58 kJ mol^{-1}, respectively, while for the LN catalyst the CH_4 and CO_2 activation energy were 32.00 kJ mol^{-1} and 25.88 kJ mol^{-1}, respectively. The results highlight the beneficial effect of partially substituting Ni with Zn in the DRM reaction, possible due to the Ni-Zn alloy, the presence of $Zn^{\delta+}$ on the surface, and oxygen vacancies formation [37]. Notably, the relatively higher activation energy for CH_4 compared to the CO_2 for both catalysts suggests that CH_4 activation is the rate-determining step (RDS) in these systems [80–82].

3.3. Spent catalysts

Although the LN catalyst was very stable and presented higher conversions than the LNZn catalyst for all temperatures tested, the spent LN catalyst showed much higher carbon deposition compared to the Zn-substituted catalyst, which can lead to carbon deactivation by blocking active surface sites or increasing the pressure and clogging.

The thermal profiles and the Raman spectra of LN and LNZn catalysts after 30 h TOS at 800 °C are shown in Fig. 7A-C. The TGA profile (Fig. 7 A) reveals an initial mass gain corresponding to the oxidation of metallic Ni, which is associated with an endothermic peak at 340 °C in the DTA analysis (Fig. 7B). Subsequently, both catalysts exhibit weight loss attributed to carbon oxidation, as evidenced by an intense DTA peak at 600 °C [37]. Notably, the LNZn catalyst shows a significantly lower weight loss (5 %) in the combustion region compared to the LN sample (50 %), indicating substantially reduced carbon accumulation.

The Raman spectra (Fig. 7 C) show three bands at 1341 cm^{-1}, 1574 cm^{-1}, and 2686 cm^{-1}, corresponding to the D, G, and 2D bands of vibration modes of carbon, respectively. The D band is attributed to breathing modes of sp^2 aromatic carbon rings and defects on carbon species; the G band is associated with the stretching of sp^2 carbon rings and chains and indicates the degree of graphitization (I_D/I_G); the 2D band is related to the second order vibrations of the D peak [37,58,63,64]. In addition, the LN catalysts exhibited high-intensity bands associated with carbon-deposited species, whereas the LNZn catalysts showed significantly lower intensities, suggesting reduced coke deposition, as confirmed by TGA.

O_2-TPO analysis was conducted to quantify the carbon deposition rate and evaluate the reactivity of the carbon deposits. The results are shown in Table 5 and Fig. S6. Firstly, the LN catalyst exhibited a significantly higher carbon formation rate - approximately 5 times greater (50 mg_{carbon} g_{cat}^{-1} h^{-1}) than that of the LNZn catalyst (10 mg_{carbon} g_{cat}^{-1} h^{-1}). Secondly, two different regions are observed on both catalysts: the first one in the temperature range of 365 °C, probably associated with the oxidation of metallic sites to NiO, as observed in the

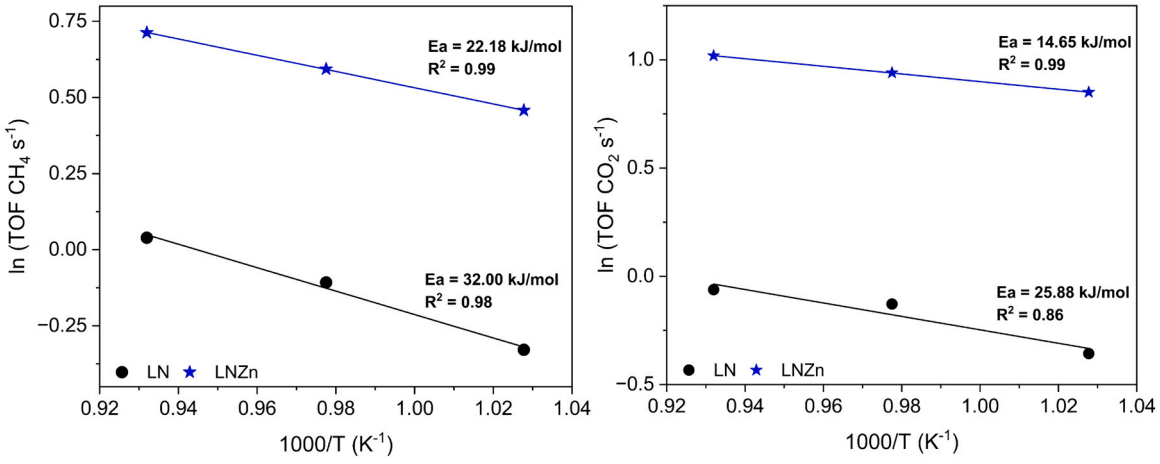

Fig. 6. Apparent activation energy of LN and LNZn.

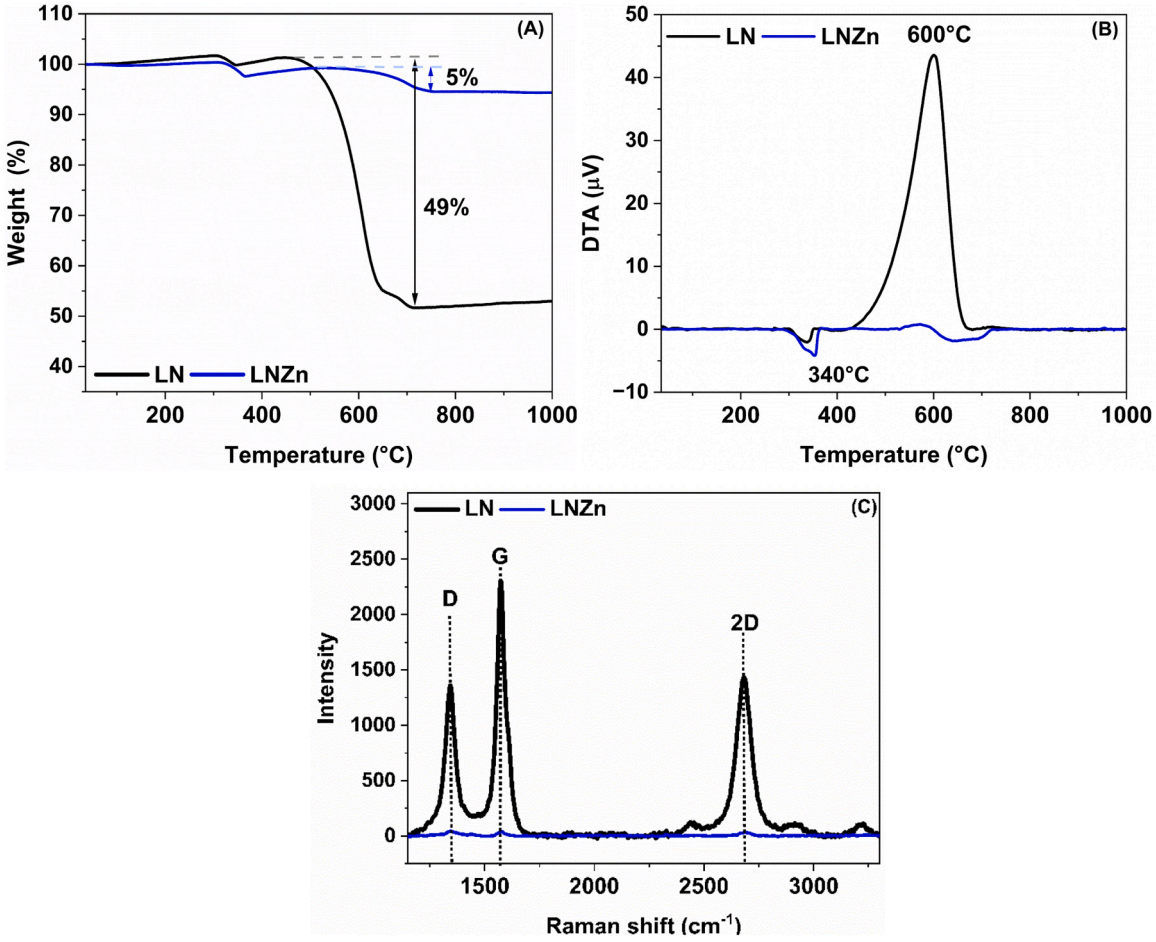

Fig. 7. TGA (A), DTA (B) and Raman spectra (C) of the spent LN and LNZn catalysts after DRM at 800 °C for 30 h.

Table 5
Ni dispersion, surface area, particle size of fresh catalyst and spent catalysts at 800 °C, and carbon formation rate at 800 °C.

Catalyst	Ni content[a] (wt%)	D_{Ni} (%)[b]	Ni Surface area (m^2/g)[b]	d_{Ni} fresh (nm)[c] *	d_{Ni} spent at 800 °C (nm)[c]	Carbon formation rate (mg_{carbon}/g_{cat}.h)[d]
LN	22.6	8.3	12.5	11.3	17.3	50
LNZn	12.6	4.4	3.7	5.3	17.4	10

* The catalysts were reduced *ex-situ* at 700 °C for 1 h in H_2 flow, simulating an *in-situ* reduction prior to the DRM reaction.
[a] Determined by ICP-OES (Fig. S5).
[b] Determined by CO-pulse chemisorption.
[c] Determined from HRTEM.
[d] Determined from TPO.

endothermic peak in DTA curve; the second region in the temperature of 545 °C to 745 °C corresponds to the oxidation of different types of carbon: such as carbon nanotubes at 545 °C and graphitic carbon (Cγ) in temperatures up to 635 °C [83], in accordance with DTA curve, which exhibits a prominent exothermic peak at this temperature range.

As shown by Fig. 8 and Table 5, HRTEM images of the LN catalyst after reduction at 700 °C exhibited metallic Ni nanoparticles evolving from the support with lattice fringes resolved at 2.21 Å and 3.24 Å corresponding to Ni (111) and La_2O_3 (222) facets, respectively (Fig. 8B), with a mean particle size of 11.3 nm by HRTEM, a Ni dispersion of 8.3 % and Ni surface area of 12.5 m^2/g. While, after reduction, LNZn catalysts resulted in the appearance of a Ni-Zn alloy on the support, as indicated by XPS (Fig. 3), with lattice fringes measured at 2.06 Å, 2.80 Å, and 3.08 Å corresponding to NiZn (111), $Zn(OH)_2$ (100), and La_2O_3 (101) planes, respectively (Fig. 8B), with a mean particle size of 5.3 nm, a Ni dispersion of 4 % and Ni surface area of 3.7 m^2/g. The substantial decrease in Ni surface area from 12.5 m^2/g in the undoped catalyst to 3.7 m^2/g in the LNZn catalyst further supports the formation of the Ni-Zn alloy, suggesting that Zn migrates to the surface and remains near the Ni-Zn alloy in the form of $Zn(OH)_2$ [37]. The formation of the metallic alloy aligns with previous reports on Ni and Zn-containing catalysts, in which Zn and Ni interact via Ni-Zn alloy formation due to their similar ionic radii [37,38,84].

After the DRM reaction at 800 °C (Fig. 8E-H), the LN catalyst exhibited a significant amount of Ni nanoparticles encapsulated by multi-walled carbon nanotubes (MWCNTs) (Fig. 8E), with an average thickness of 9 nm (± 3.5 nm) and length of 30 nm (± 11 nm). According to Shoji et al. [85], Ni nanoparticles that migrate freely across the support act as catalysts for MWCNT growth by dissolving carbon from the gaseous atmosphere, followed by carbon recrystallization on the Ni surface in the form of CNTs. This mechanism may explain the substantial formation of MWCNTs observed on the LN catalyst. Additionally, an onion-shell structure composed of graphitic carbon layers was formed (Fig. 8G), exhibiting 27 graphene sheets with an interlayer spacing of 0.4 nm.

Compared to the undoped catalyst, the LNZn catalyst exhibited fewer Ni particles removed from the support and encapsulated within carbon nanotubes; the average thickness and length of the nanotubes were found to be 10 nm (± 1.7 nm) and 7 nm (± 8.5 nm), respectively (Fig. 8F). Notably, an increase in particle size from 5.3 nm to 17 nm was observed in the LNZn catalyst after the reaction at 800 °C, suggesting

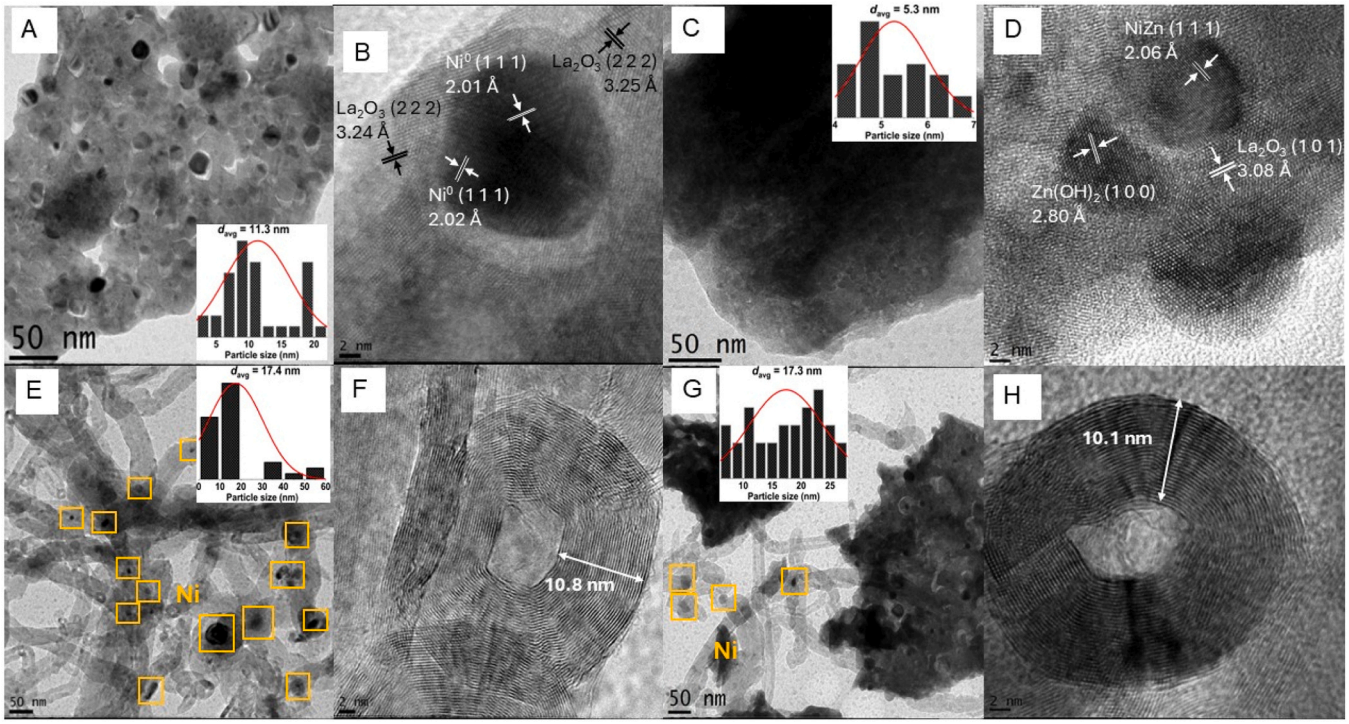

Fig. 8. (A-D) HRTEM images of LN and LNZn catalysts after H_2 reduction at 700 °C, simulating an in-situ reduction prior to DRM reaction. Particle size distribution (A) and lattice fringes of reduced LN; particle size distribution (C) and lattice fringes of the reduced LNZn (D). E-H HRTEM images of post DRM reaction at 800 °C. (E) LN catalyst shows encapsulated ni particles in carbon nanotubes. (F) Carbon formed after DRM on LN. G) LNZn catalyst shows almost no ni particles encapsulated by carbon nanotubes. (H) Carbon formed after DRM on LNZn.

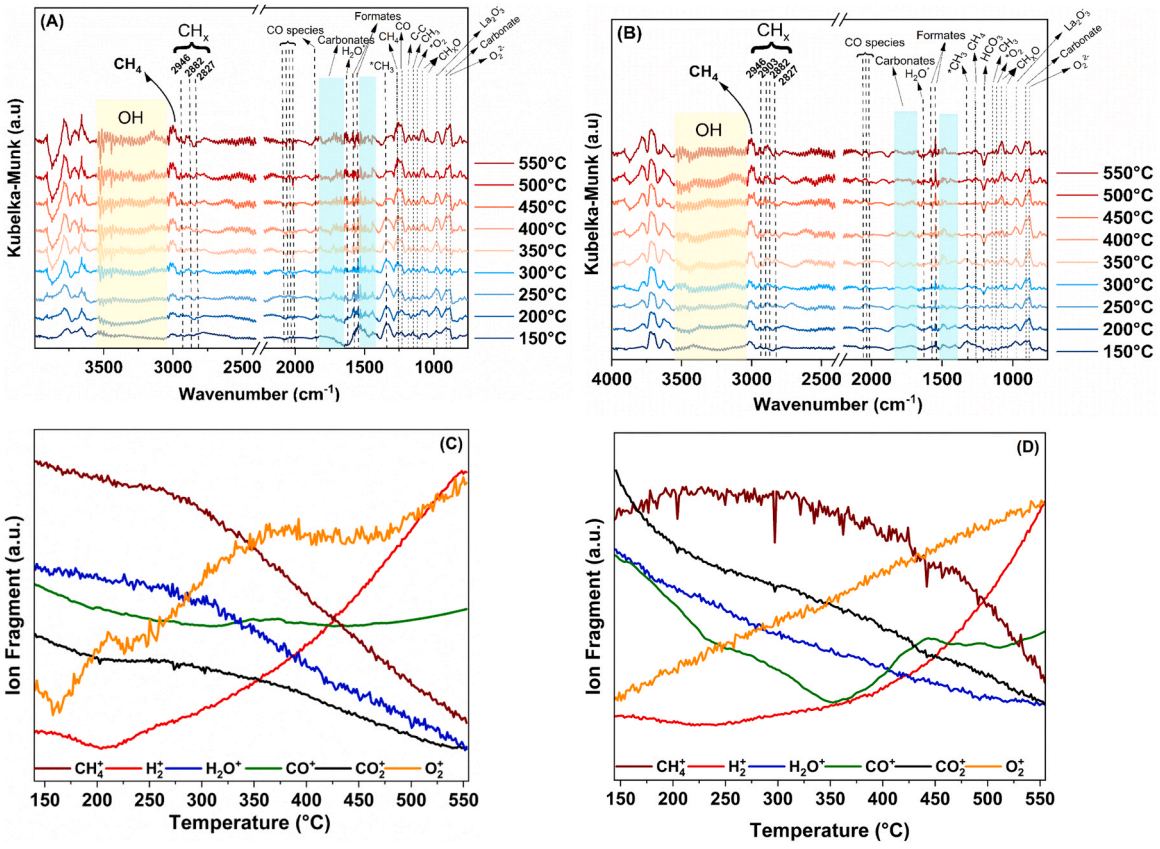

Fig. 9. *Quasi-in-situ* DRIFTS-MS studies of reduced catalysts LN (A and C) and LNZn (B and D) at different temperatures. CH_4, H_2, H_2O, CO, CO_2 and O_2 fragments were monitored by MS.

that $Zn(OH)_2$, initially located near the alloy (Fig. 8D), migrates from the boundary into the alloy structure. This migration leads to significant particle growth while improving the structural stability of the active phase on the support. Such stabilization effectively mitigates coke formation and prevents the removal and encapsulation of Ni particles by carbon nanotubes [37].

3.4. Mechanism study of DRM using quasi-in-situ DRIFTS-MS

Quasi-in-situ DRIFTS-MS results are depicted in Fig. 9A-D. As observed in Fig. 9A-B, the LN and LNZn catalysts exhibit different intensities characteristic bands in the regions associated with carbonate species (900, 1410–1530 cm^{-1} and 1721–1817 cm) [51,86–88]. With increasing temperature, the LN catalyst displays an increase of bands related to carbonate species, primarily due to the presence of $La_2O_2CO_3$. In contrast, the LNZn catalyst does not exhibit the same behavior in consistent agreement with CO_2-TPD results at mid-range. temperatures Notably, the increase in temperature leads to a rise in the intensity of the gaseous CH_4 deformation vibration bands (3015 cm^{-1} and 1261 cm^{-1}) for both catalysts [89,90]. Simultaneously, increasing temperature facilitated methane cracking via CH_x intermediates, as evidenced by the appearance of bands corresponding to CH_x symmetric stretching in the 2946–2827 cm^{-1} range [89]. This phenomenon can be verified by the mass spectra recorded during *quasi-in-situ* DRIFTS analysis (Fig. 9C-D), showing an increase in the ion fragment related to H_2^+ and a decrease to CH_4^+. It is noted that, in the presence of CO_2, the CH_4 cracking point changes to lower temperatures compared to CH_4-TPSR due to the soft oxidizing nature of CO_2. Consequently, CO^+ ion fragment increases significantly in temperatures up to 300 °C, resulting in CO characteristic bands in 1231, 2017, 2036, and 2058 cm^{-1}, identified as CO asymmetric stretching vibrations, linear CO absorbed in Ni, and CO symmetric stretching vibrations, respectively [59,87,91,92].

Notably, the LNZn catalyst exhibited a temperature-dependent increase in characteristic bands associated with bicarbonate HCO_3^-, formates ($HCOO^-$), and CH_xO species, observed at 1205, 1547–1581, and 1042–1078 cm^{-1}, respectively [59,86,89,93]. The formation of HCO_3^- and $HCOO^-$ is related to the CO_2 activation, leading to $CO_2^{\delta-}$ on the vacancy site which can react with adsorbed *H, OH^- (3100–3500 cm^{-1}), or with adsorbed oxygen species [59,86,87]. Additionally, HCO_3^- can further react with adsorbed H species to form $HCOO^-$, which decomposes to CO [79]. Meanwhile, CH_xO species are related to the interaction between adsorbed oxygen species with CH_x derived from CH_4 disproportionation [89]. The occurrence of oxygen-containing intermediary species is attributed to the higher oxophilicity of Zn in the LNZn catalyst, facilitating carbon gasification [38]. In contrast, for the LN catalyst, although CH_xO and $HCOO^-$ bands were detected, their intensity remained unchanged with increasing temperature, suggesting carbonaceous species accumulation, as evidenced by the emergence of the C–C band at 1177 cm^{-1} [94].

Mass spectrometry analysis revealed distinct trends in O_2^+ ion evolution for the catalysts. The LNZn catalyst exhibited a continuous increase in O_2^+ intensity with temperature, whereas the LN catalyst showed an increase between 250 and 400 °C and a decrease at higher temperatures. This behavior indicates that oxygen species improved the formation of oxygen-containing compounds, such as formates, bicarbonates, and bridge-type oxygen species (O_2^{2-}, 880 cm^{-1}), which are related to the surface sites [61]. The presence of the NiZn alloy in the LNZn catalyst enhances surface oxygen vacancies, structural defects, and metal-support interactions, which are closely associated with the oxygen storage capacity and mobility in the catalysts. These defects are crucial in facilitating in-situ carbon gasification via oxidation pathways, leading to superior CO formation [37,95], as verified in the 30 h TOS in the LNZn catalyst.

Based on the characterization and *quasi-in-situ* DRIFTS-MS results, we propose a mechanism for the LNZn catalyst during DRM reaction (Fig. 10). CH_4 dissociates at NiZn sites, forming CH_x species, which

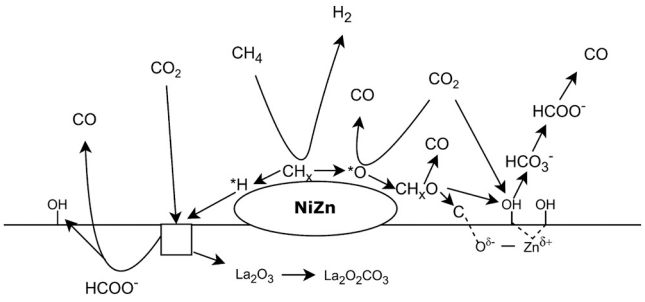

Fig. 10. Proposed DRM reaction mechanism for LNZn catalyst based on characterization and quasi in-situ DRIFTS-MS results. Square denotes a vacancy.

subsequently react with oxygen species derived from CO_2 activation at the alloy interface, leading to CH_xO formation. These intermediates further decompose into H_2 and CO. CO_2 activation on oxygen vacancies and adsorbed O* species generates CH_xO, HCO_3^-, and $HCOO^-$, which decompose into syngas and hydroxyl species on the catalyst surface. At higher temperatures (>500 °C), CO_2 is also chemically activated on La_2O_3, forming $La_2O_2CO_3$, as confirmed by CO_2-TPD analysis. The proposed DRM mechanism aligns well with literature reports on Ni and Ni-metal alloy catalysts, and La_2O_3-ZnO-based supports [89,95,96], highlighting the crucial role of oxygen-containing species in carbon oxidation during DRM and clearing the superior anti-carbon behavior of the LNZn catalyst.

4. Conclusions

In summary, perovskite-type oxides LN and LNZn were synthesized using the polymeric precursor method to investigate the synergistic effect of Zn incorporation into the Ni site on oxygen mobility and carbon formation during the DRM reaction. CH_4-TPSR-MS and H_2-TPHR-MS analyses confirmed the generation of oxygen-containing species (H_2O, CO, O_2, and CO_2), indicating enhanced oxygen mobility in the Zn-promoted catalyst. HRTEM and XPS results revealed the formation of a Ni-Zn alloy, which induces oxygen vacancies and structural defects, facilitating carbon removal due to the higher oxophilicity of Zn. *Quasi-in-situ* DRIFTS-MS demonstrated that the DRM mechanism over the LNZn catalyst involves CH_4 activation on NiZn sites. In contrast, CO_2 activation occurs both on the support and active sites, leading to the formation of intermediate species (CH_xO, $HCOO^-$, and HCO_3^-), which promote carbon gasification and CO formation. Post-reaction analyses confirmed the superior anti-carbon properties of LNZn, highlighting the positive synergistic effect of Zn incorporation in mitigating carbon deposition.

CRediT authorship contribution statement

Assaf Elisabete: Writing – review & editing, Visualization, Validation, Methodology. **Martin Schmal:** Writing – review & editing, Visualization, Validation, Supervision, Methodology, Conceptualization. **Juliana Bertoldi:** Writing – review & editing, Writing – original draft, Visualization, Validation, Methodology, Investigation, Conceptualization. **Morgana Rosset:** Writing – review & editing, Writing – original draft, Methodology. **Larissa Otubo:** Writing – review & editing, Visualization, Validation, Methodology. **Camila E. Kozonoe:** Writing – review & editing, Visualization, Methodology. **Oliveira Éder:** Writing – review & editing, Visualization, Methodology.

Declaration of Competing Interest

The authors declare that they have no known competing financial interests or personal relationships that could have appeared to influence the work reported in this paper.

Acknowledgments

This study was financed in part by the Coordenação de Aperfeiçoamento de Pessoal de Nível Superior - Brasil (CAPES) - Finance Code 001 and by Conselho Nacional de Desenvolvimento Científico e Tecnológico (CNPq) Process Number 156589/2022–2.

Appendix A. Supporting information

Supplementary data associated with this article can be found in the online version at doi:10.1016/j.apcata.2025.120400.

Data availability

No data was used for the research described in the article.

References

[1] L. Xu, W. Liu, X. Zhang, L. Tao, L. Xia, X. Xu, J. Song, W. Zhou, X. Fang, X. Wang, Ni/La 2 o 3 catalysts for dry reforming of methane: insights into the factors improving the catalytic performance, ChemCatChem 11 (2019) 2887–2899, https://doi.org/10.1002/cctc.201900331.

[2] Q. Huang, X. Fang, Q. Cheng, Q. Li, X. Xu, L. Xu, W. Liu, Z. Gao, W. Zhou, X. Wang, Synthesis of a highly active and stable Nickel-Embedded alumina catalyst for methane dry reforming: on the confinement effects of alumina shells for nickel nanoparticles, ChemCatChem 9 (2017) 3563–3571, https://doi.org/10.1002/cctc.201700490.

[3] R. Carapellucci, L. Giordano, Steam, dry and autothermal methane reforming for hydrogen production: a thermodynamic equilibrium analysis, J. Power Sources 469 (2020) 228391, https://doi.org/10.1016/j.jpowsour.2020.228391.

[4] A.M. Gadalla, B. Bower, The role of catalyst support on the activity of nickel for reforming methane with CO2, Chem. Eng. Sci. 43 (1988) 3049–3062, https://doi.org/10.1016/0009-2509(88)80058-7.

[5] A.M. Ranjekar, G.D. Yadav, Dry reforming of methane for syngas production: a review and assessment of catalyst development and efficacy, J. Indian Chem. Soc. 98 (2021) 100002, https://doi.org/10.1016/j.jics.2021.100002.

[6] G.C. de Araujo, S.M. de Lima, J.M. Assaf, M.A. Peña, J.L.G. Fierro, M. do Carmo Rangel, Catalytic evaluation of perovskite-type oxide LaNi1−xRuxO3 in methane dry reforming, Catal. Today (2008) 129–135, https://doi.org/10.1016/J.CATTOD.2007.12.049, 133135.

[7] J. Kehres, J.G. Jakobsen, J.W. Andreasen, J.B. Wagner, H. Liu, A. Molenbroek, J. Sehested, I. Chorkendorff, T. Vegge, Dynamical properties of a Ru/MgAl 2 o 4 catalyst during reduction and dry methane reforming, J. Phys. Chem. C. 116 (2012) 21407–21415, https://doi.org/10.1021/jp3069656.

[8] A. Abdulrasheed, A.A. Jalil, Y. Gambo, M. Ibrahim, H.U. Hambali, M.Y. Shahul Hamid, A review on catalyst development for dry reforming of methane to syngas: recent advances, Renew. Sustain. Energy Rev. 108 (2019) 175–193, https://doi.org/10.1016/j.rser.2019.03.054.

[9] W.N. Manan, W.N.R. Wan Isahak, Z. Yaakob, CeO2-Based heterogeneous catalysts in dry reforming methane and steam reforming methane: a short review, Catalysts 12 (2022) 452, https://doi.org/10.3390/catal12050452.

[10] L.A. Arkatova, The deposition of coke during carbon dioxide reforming of methane over intermetallides, Catal. Today 157 (2010) 170–176, https://doi.org/10.1016/j.cattod.2010.03.003.

[11] Q. Zhu, Y. Liu, X. Qin, L. Liu, Z. Ren, X. Tao, C. Wang, H. Wang, L. Li, X. Liu, L. Chen, L. Wang, Zeolite fixed cobalt – nickel nanoparticles for coking and sintering resistance in dry reforming of methane, Chem. Eng. Sci. 280 (2023) 119030, https://doi.org/10.1016/j.ces.2023.119030.

[12] L. Huang, D. Li, D. Tian, L. Jiang, Z. Li, H. Wang, K. Li, Optimization of Ni-Based catalysts for dry reforming of methane via alloy design: a review, Energy Fuels 36 (2022) 5102–5151, https://doi.org/10.1021/acs.energyfuels.2c00523.

[13] K. Wittich, M. Krämer, N. Bottke, S.A. Schunk, Catalytic dry reforming of methane: insights from model systems, ChemCatChem 12 (2020) 2130–2147, https://doi.org/10.1002/cctc.201902142.

[14] M. Schmal, F.S. Toniolo, C.E. Kozonoe, Perspective of catalysts for (Tri) reforming of natural gas and flue gas rich in CO2, Appl. Catal. A Gen. 568 (2018) 23–42, https://doi.org/10.1016/j.apcata.2018.09.017.

[15] N. El Hassan, M.N. Kaydouh, H. Geagea, H. El Zein, K. Jabbour, S. Casale, H. El Zakhem, P. Massiani, Low temperature dry reforming of methane on rhodium and cobalt based catalysts: active phase stabilization by confinement in mesoporous SBA-15, Appl. Catal. A Gen. 520 (2016) 114–121, https://doi.org/10.1016/j.apcata.2016.04.014.

[16] Z. Qin, J. Chen, X. Xie, X. Luo, T. Su, H. Ji, CO2 reforming of CH4 to syngas over nickel-based catalysts, Environ. Chem. Lett. 18 (2020) 997–1017, https://doi.org/10.1007/s10311-020-00996-w.

[17] C. Jensen, M.S. Duyar, Thermodynamic analysis of dry reforming of methane for valorization of landfill gas and natural gas, Energy Technol. 9 (2021) 2100106, https://doi.org/10.1002/ente.202100106.

[18] P. Delir Kheyrollahi Nezhad, M.F. Bekheet, N. Bonmassar, A. Gili, F. Kamutzki, A. Gurlo, A. Doran, S. Schwarz, J. Bernardi, S. Praetz, A. Niaei, A. Farzi, S. Penner, Elucidating the role of earth alkaline doping in perovskite-based methane dry reforming catalysts, Catal. Sci. Technol. 12 (2022) 1229–1244, https://doi.org/10.1039/D1CY02044G.

[19] J. Guo, H. Lou, H. Zhao, D. Chai, X. Zheng, Dry reforming of methane over nickel catalysts supported on magnesium aluminate spinels, Appl. Catal. A Gen. 273 (2004) 75–82, https://doi.org/10.1016/j.apcata.2004.06.014.

[20] Z. Bian, Z. Wang, B. Jiang, P. Hongmanorom, W. Zhong, S. Kawi, A review on perovskite catalysts for reforming of methane to hydrogen production, Renew. Sustain. Energy Rev. 134 (2020) 110291, https://doi.org/10.1016/j.rser.2020.110291.

[21] C. Moure, O. Peña, Recent advances in perovskites: processing and properties, Prog. Solid State Chem. 43 (2015) 123–148, https://doi.org/10.1016/j.progsolidstchem.2015.09.001.

[22] N. Bonmassar, M.F. Bekheet, L. Schlicker, A. Gili, A. Gurlo, A. Doran, Y. Gao, M. Heggen, J. Bernardi, B. Klötzer, S. Penner, In Situ-Determined catalytically active state of LaNiO3 in methane dry reforming, ACS Catal. 10 (2020) 1102–1112, https://doi.org/10.1021/acscatal.9b03687.

[23] M.A. Salaev, L.F. Liotta, O.V. Vodyankina, Lanthanoid-containing Ni-based catalysts for dry reforming of methane: a review, Int J. Hydrog. Energy 47 (2022) 4489–4535, https://doi.org/10.1016/j.ijhydene.2021.11.086.

[24] K.T.C. Roseno, R. Brackmann, M.A. da Silva, M. Schmal, Investigation of LaCoO3, LaFeO3 and LaCo0.5Fe0.5O3 perovskites as catalyst precursors for syngas production by partial oxidation of methane, Int J. Hydrog. Energy 41 (2016) 18178–18192, https://doi.org/10.1016/j.ijhydene.2016.07.207.

[25] D. Ferri, L. Forni, Methane combustion on some perovskite-like mixed oxides, Appl. Catal. B 16 (1998) 119–126, https://doi.org/10.1016/S0926-3373(97)00065-9.

[26] G. Valderrama, A. Kiennemann, M.R. Goldwasser, Dry reforming of CH4 over solid solutions of LaNi1-xCoxO3, Catal. Today (2008) 142–148, https://doi.org/10.1016/j.cattod.2007.12.069, 133135.

[27] G. Valderrama, A. Kiennemann, C.U. de Navarro, M.R. Goldwasser, LaNi1-xMnxO3 perovskite-type oxides as catalysts precursors for dry reforming of methane, Appl. Catal. A Gen. 565 (2018) 26–33, https://doi.org/10.1016/j.apcata.2018.07.039.

[28] X. Cui, T. Wu, J.P. Cao, W. Tang, F.L. Yang, B.A. Zhu, Z. Wang, Mechanism for catalytic cracking of coal tar over fresh and reduced LaNi1-xFexO3 perovskite, Fuel 288 (2021) 119683, https://doi.org/10.1016/J.FUEL.2020.119683.

[29] D.D. Sarma, O. Rader, T. Kachel, A. Chainani, M. Mathew, K. Holldack, W. Gudat, W. Eberhardt, Contrasting behavior of homovalent-substituted and hole-doped systems: o K-edge spectra from LaNi1-xMxO3 (M=Mn, Fe, and Co) and La1-xSrxMnO3, Phys. Rev. B 49 (1994) 14238–14243, https://doi.org/10.1103/PhysRevB.49.14238.

[30] G.C. de Araujo, S.M. de Lima, J.M. Assaf, M.A. Peña, J.L.G. Fierro, M. do Carmo Rangel, Catalytic evaluation of perovskite-type oxide LaNi1−xRuxO3 in methane dry reforming, Catal. Today 133 135 (2008) 129–135, https://doi.org/10.1016/J.CATTOD.2007.12.049.

[31] G.R. Moradi, F. Khosravian, M. Rahmanzadeh, Effects of partial substitution of ni by cu in LaNiO 3 perovskite catalyst for dry methane reforming, Chin. J. Catal. 33 (2012) 797–801, https://doi.org/10.1016/S1872-2067(11)60378-1.

[32] X. Xu, Y. Zhong, Z. Shao, Double perovskites in catalysis, electrocatalysis, and Photo(electro)catalysis, Trends Chem. 1 (2019) 410–424, https://doi.org/10.1016/j.trechm.2019.05.006.

[33] A.S. Al-Fatesh, Y. Arafat, A.A. Ibrahim, S.O. Kasim, A. Alharthi, A.H. Fakeeha, A. E. Abasaeed, G. Bonura, F. Frusteri, Catalytic behaviour of Ce-Doped ni systems supported on stabilized zirconia under dry reforming conditions, Catalysts 9 (2019) 473, https://doi.org/10.3390/catal9050473.

[34] S. Bhattar, A. Krishnakumar, S. Kanitkar, A. Abedin, D. Shekhawat, D.J. Haynes, J. J. Spivey, Dry reforming of methane over Ni- and Sr-Substituted lanthanum zirconate pyrochlore catalysts: effect of ni loading, Ind. Eng. Chem. Res. 58 (2019) 19386–19396, https://doi.org/10.1021/acs.iecr.9b02434.

[35] Y. Ma, Y. Ma, Y. Chen, S. Ma, Q. Li, X. Hu, Z. Wang, C.E. Buckley, D. Dong, Highly stable nanofibrous La2NiZrO6 catalysts for fast methane partial oxidation, Fuel 265 (2020) 116861, https://doi.org/10.1016/j.fuel.2019.116861.

[36] G.R. Moradi, M. Rahmanzadeh, F. Khosravian, The effects of partial substitution of ni by zn in LaNiO3 perovskite catalyst for methane dry reforming, J. CO2 Util. 6 (2014) 7–11, https://doi.org/10.1016/j.jcou.2014.02.001.

[37] V.K. Velisoju, Q.J.S. Virpurwala, Y. Attada, X. Bai, B. Davaasuren, M. Ben Hassine, X. Yao, G. Lezcano, S.R. Kulkarni, P. Castano, Overcoming the kinetic and deactivation limitations of ni catalyst by alloying it with zn for the dry reforming of methane, J. CO2 Util. 75 (2023) 102573, https://doi.org/10.1016/j.jcou.2023.102573.

[38] A. Chatla, F. Abu-Rub, A.V. Prakash, G. Ibrahim, N.O. Elbashir, Highly stable and coke-resistant Zn-modified Ni-Mg-Al hydrotalcite derived catalyst for dry reforming of methane: synergistic effect of ni and zn, Fuel 308 (2022), https://doi.org/10.1016/j.fuel.2021.122042.

[39] J. Bertoldi, K.T. de Campos Roseno, M. Schmal, V.D. Lage, G.G.G.G. Lenzi, R. Brackmann, La1−x(Ce, Sr)x NiO3 perovskite-type oxides as catalyst precursors to syngas production through tri-reforming of methane, Int J. Hydrog. Energy 47 (2022) 31279–31294, https://doi.org/10.1016/j.ijhydene.2022.07.053.

[40] M. Akri, S. Zhao, X. Li, K. Zang, A.F. Lee, M.A. Isaacs, W. Xi, Y. Gangarajula, J. Luo, Y. Ren, Y.T. Cui, L. Li, Y. Su, X. Pan, W. Wen, Y. Pan, K. Wilson, L. Li, B. Qiao, H. Ishii, Y.F. Liao, A. Wang, X. Wang, T. Zhang, Atomically dispersed nickel as coke-resistant active sites for methane dry reforming, 1–10, Nat. Commun. 2019 10 (2019) 1–10, https://doi.org/10.1038/s41467-019-12843-w.

[41] M. Schmal, C.A.C. Perez, R.N.S.H. Magalhães, Synthesis and characterization of perovskite-type oxides la 1-xMxCoO3 (M = Ce, Sr) for the selective co oxidation (SELOX), Top. Catal. 57 (2014) 1103–1111, https://doi.org/10.1007/s11244-014-0275-7.

[42] H. Fjellvåg, O.H. Hansteen, B.G. Tilset, A. Olafsen, N. Sakai, H. Seim, Thermal analysis as an aid in the synthesis of non-stoichiometric perovskite type oxides, Thermochim. Acta 256 (1995) 75–89, https://doi.org/10.1016/0040-6031(94)02220-I.
[43] E. Haibel, E. Füglein, A.S. Schulze, D. Walter, Thermal decomposition of carbonated lanthanum hydroxide, J. Therm. Anal. Calor. 138 (2019) 3571–3575, https://doi.org/10.1007/s10973-019-08461-9.
[44] C. Chu, Y. Zhao, S. Li, Y. Sun, Correlation between the acid-base properties of the La2O3 catalyst and its methane reactivity, Phys. Chem. Chem. Phys. 18 (2016) 16509–16517, https://doi.org/10.1039/c6cp02459a.
[45] J. Shao, G. Zeng, Y. Li, Effect of zn substitution to a LaNiO3−Δ perovskite structured catalyst in ethanol steam reforming, Int J. Hydrog. Energy 42 (2017) 17362–17375, https://doi.org/10.1016/j.ijhydene.2017.04.066.
[46] L. Minervini, R.W. Grimes, J.A. Kilner, K.E. Sickafus, Oxygen migration in La2NiO(4+δ), J. Mater. Chem. 10 (2000) 2349–2354, https://doi.org/10.1039/b004212i.
[47] R.J. Woolley, B.N. Illy, M.P. Ryan, S.J. Skinner, In situ determination of the nickel oxidation state in la 2NiO4+δ and La4Ni3O 10-δ using X-ray absorption near-edge structure, J. Mater. Chem. 21 (2011) 18592–18596, https://doi.org/10.1039/c1jm14320d.
[48] S. Ponce, M.A. Peña, J.L.G. Fierro, Surface properties and catalytic performance in methane combustion of SR-substituted lanthanum manganites, Appl. Catal. B 24 (2000) 193–205, https://doi.org/10.1016/S0926-3373(99)00111-3.
[49] K. Li, X. Chang, C. Pei, X. Li, S. Chen, X. Zhang, S. Assabumrungrat, Z.-J. Zhao, L. Zeng, J. Gong, Ordered mesoporous Ni/La2O3 catalysts with interfacial synergism towards CO2 activation in dry reforming of methane, Appl. Catal. B 259 (2019) 118092, https://doi.org/10.1016/j.apcatb.2019.118092.
[50] S. Singh, D. Zubenko, B.A. Rosen, Influence of LaNiO 3 shape on its Solid-Phase crystallization into Coke-Free reforming catalysts, ACS Catal. 6 (2016) 4199–4205, https://doi.org/10.1021/acscatal.6b00673.
[51] Y. Dai, M. Xu, Q. Wang, R. Huang, Y. Jin, B. Bian, C. Tumurbaatar, B. Ishtsog, T. Bold, Y. Yang, Enhanced activity and stability of Ni/La2O2CO3 catalyst for CO2 methanation by metal-carbonate interaction, Appl. Catal. B 277 (2020) 119271, https://doi.org/10.1016/j.apcatb.2020.119271.
[52] X. Song, X. Dong, S. Yin, M. Wang, M. Li, H. Wang, Effects of fe partial substitution of La2NiO4/LaNiO3 catalyst precursors prepared by wet impregnation method for the dry reforming of methane, Appl. Catal. A Gen. 526 (2016) 132–138, https://doi.org/10.1016/j.apcata.2016.07.024.
[53] P. Cao, P. Tang, M.F. Bekheet, H. Du, L. Yang, L. Haug, A. Gili, B. Bischoff, A. Gurlo, M. Kunz, R.E. Dunin-Borkowski, S. Penner, M. Heggen, Atomic-Scale insights into nickel exsolution on LaNiO3 catalysts via in situ electron microscopy, J. Phys. Chem. C 126 (2022) 786–796, https://doi.org/10.1021/acs.jpcc.1c09257.
[54] A. Shahnazi, S. Firoozi, Improving the catalytic performance of LaNiO3perovskite by manganese substitution via ultrasonic spray pyrolysis for dry reforming of methane, J. CO2 Util. 45 (2021) 101455, https://doi.org/10.1016/j.jcou.2021.101455.
[55] S. Ewald, O. Hinrichsen, On the interaction of CO2 with Ni-Al catalysts, Appl. Catal. A Gen. 580 (2019) 71–80, https://doi.org/10.1016/j.apcata.2019.04.005.
[56] B.C. da Silva, P.H.C. Bastos, R.B.S. Junior, N.R. Checca, D.S. Costa, R. Fréty, S. T. Brandão, Oxy-CO2 reforming of CH4 on Ni-based catalysts: evaluation of cerium and aluminum addition on the structure and properties of the reduced materials, Catal. Today 381 (2021) 50–64, https://doi.org/10.1016/j.cattod.2020.09.004.
[57] M. Zhang, J. Zhang, Z. Zhou, S. Chen, T. Zhang, F. Song, Q. Zhang, N. Tsubaki, Y. Tan, Y. Han, Effects of the surface adsorbed oxygen species tuned by rare-earth metal doping on dry reforming of methane over Ni/ZrO2 catalyst, Appl. Catal. B 264 (2020) 118522, https://doi.org/10.1016/J.APCATB.2019.118522.
[58] M. Zhang, J. Zhang, Y. Wu, J. Pan, Q. Zhang, Y. Tan, Y. Han, Insight into the effects of the oxygen species over Ni/ZrO2 catalyst surface on methane reforming with carbon dioxide, Appl. Catal. B 244 (2019) 427–437, https://doi.org/10.1016/j.apcatb.2018.11.068.
[59] S. Bai, F. Liu, B. Huang, F. Li, H. Lin, T. Wu, M. Sun, J. Wu, Q. Shao, Y. Xu, X. Huang, High-efficiency direct methane conversion to oxygenates on a cerium dioxide nanowires supported rhodium single-atom catalyst, Nat. Commun. 11 (2020) 954, https://doi.org/10.1038/s41467-020-14742-x.
[60] S.F. Moya, R.L. Martins, M. Schmal, Monodispersed and nanostructrured Ni/SiO2 catalyst and its activity for non oxidative methane activation, Appl. Catal. A Gen. 396 (2011) 159–169, https://doi.org/10.1016/j.apcata.2011.02.007.
[61] J. Xu, T. Zhang, S. Fang, J. Li, Z. Wu, W. Wang, J. Zhu, E. Gao, S. Yao, Exploring the roles of oxygen species in H2 oxidation at β-MnO2 surfaces using operando DRIFTS-MS, Commun. Chem. 5 (2022) 97, https://doi.org/10.1038/s42004-022-00717-0.
[62] M. Behrens, F. Studt, I. Kasatkin, S. Kühl, M. Hävecker, F. Abild-Pedersen, S. Zander, F. Girgsdies, P. Kurr, B.-L. Kniep, M. Tovar, R.W. Fischer, J.K. Nørskov, R. Schlögl, The active site of methanol synthesis over Cu/ZnO/Al2O3 industrial catalysts, Science 336 (1979) (2012) 893–897, https://doi.org/10.1126/science.1219831.
[63] A.C. Ferrari, Raman spectroscopy of graphene and graphite: disorder, electron–phonon coupling, doping and nonadiabatic effects, Solid State Commun. 143 (2007) 47–57, https://doi.org/10.1016/j.ssc.2007.03.052.
[64] A.C. Ferrari, J. Robertson, Resonant Raman spectroscopy of disordered, amorphous, and diamondlike carbon, Phys. Rev. B Condens Matter Mater. Phys. 64 (2001) 1–13, https://doi.org/10.1103/PhysRevB.64.075414.
[65] R.C. Rabelo-Neto, H.B.E. Sales, C.V.M. Inocêncio, E. Varga, A. Oszko, A. Erdohelyi, F.B. Noronha, L.V. Mattos, CO2 reforming of methane over supported LaNiO3 perovskite-type oxides, Appl. Catal. B 221 (2018) 349–361, https://doi.org/10.1016/j.apcatb.2017.09.022.
[66] S. Mickevičius, S. Grebinskij, V. Bondarenka, B. Vengalis, K. Šliužienė, B. A. Orlowski, V. Osinniy, W. Drube, Investigation of epitaxial LaNiO3−x thin films by high-energy XPS, J. Alloy. Compd. 423 (2006) 107–111, https://doi.org/10.1016/j.jallcom.2005.12.038.
[67] E.P. Komarala, I. Komissarov, B.A. Rosen, Effect of fe and mn substitution in LaNiO3 on exsolution, activity, and stability for methane dry reforming, Catalysts 2020 10 (2019) 27, https://doi.org/10.3390/CATAL10010027.
[68] S. Wasantwisut, C. Brea, S. Jo, B.H. Arpini, G. Hu, K.L. Gilliard-AbdulAziz, Regenerable Ni-Au/La2O3 catalysts for dry reforming of methane, Appl. Catal. O Open 194 (2024) 206990, https://doi.org/10.1016/J.APCATO.2024.206990.
[69] M.A.A. Aziz, A.A. Jalil, S. Wongsakulphasatch, D.V.N. Vo, Understanding the role of surface basic sites of catalysts in CO2 activation in dry reforming of methane: a short review, Catal. Sci. Technol. 10 (2020) 35–45, https://doi.org/10.1039/C9CY01519A.
[70] F. Morales Anzures, P. Salinas Hernández, G. Mondragón Galicia, A. Gutiérrez Martínez, F. Tzompantzi Morales, M.A. Romero Romo, R. Pérez Hernández, Synthetic gas production by dry reforming of methane over Ni/Al2O3–ZrO2 catalysts: high H2/CO ratio, Int J. Hydrog. Energy 46 (2021) 26224–26233, https://doi.org/10.1016/j.ijhydene.2021.05.073.
[71] A. Manabayeva, P. Mäki-Arvela, Z. Vajglová, M. Martinez-Klimov, O. Yevdokimova, A. Peuronen, M. Lastusaari, T. Tirri, K. Kassymkan, T. S. Baizhumanova, M. Zhumabek, R.O. Sarsenova, Z.T. Zheksenbaeva, G. N. Kaumenova, V. Russo, D.Y. Murzin, S.A. Tungatarova, Dry reforming of methane over rare-earth metal oxide Ni-M-Al (M = Ce, La) catalysts, Ind. Eng. Chem. Res. 62 (2023) 20588–20607, https://doi.org/10.1021/ACS.IECR.3C02341/ASSET/IMAGES/MEDIUM/IE3C02341_M031.GIF.
[72] N. Wang, K. Shen, L. Huang, X. Yu, W. Qian, W. Chu, Facile route for synthesizing ordered mesoporous Ni-Ce-Al oxide materials and their catalytic performance for methane dry reforming to hydrogen and syngas, ACS Catal. 3 (2013) 1638–1651, https://doi.org/10.1021/CS4003113/ASSET/IMAGES/LARGE/CS-2013-003113_0014.JPEG.
[73] H. Peng, X. Zhang, X. Han, X. You, S. Lin, H. Chen, W. Liu, X. Wang, N. Zhang, Z. Wang, P. Wu, H. Zhu, S. Dai, Catalysts in coronas: a surface spatial confinement strategy for High-Performance catalysts in methane dry reforming, ACS Catal. 9 (2019) 9072–9080, https://doi.org/10.1021/ACSCATAL.9B00968/ASSET/IMAGES/LARGE/CS-2019-009685_0007.JPEG.
[74] C. Chen, X. Wang, H. Huang, X. Zou, F. Gu, F. Su, X. Lu, Synthesis of mesoporous Ni–La–Si mixed oxides for CO2 reforming of CH4 with a high H2 selectivity, Fuel Process. Technol. 185 (2019) 56–67, https://doi.org/10.1016/J.FUPROC.2018.11.017.
[75] A.M. Manabayeva, P. Mäki-Arvela, Z. Vajglová, M. Martinéz-Klimov, T. Tirri, T. S. Baizhumanova, V.P. Grigor'eva, M. Zhumabek, Y.A. Aubakirov, I.L. Simakova, D.Y. Murzin, S.A. Tungatarova, Dry reforming of methane over Ni-Fe-Al catalysts prepared by solution combustion synthesis, Ind. Eng. Chem. Res. 62 (2023) 11439–11455, https://doi.org/10.1021/ACS.IECR.3C00272/ASSET/IMAGES/MEDIUM/IE3C00272_M022.GIF.
[76] N. Wang, K. Shen, L. Huang, X. Yu, W. Qian, W. Chu, Facile route for synthesizing ordered mesoporous Ni-Ce-Al oxide materials and their catalytic performance for methane dry reforming to hydrogen and syngas, ACS Catal. 3 (2013) 1638–1651, https://doi.org/10.1021/CS4003113/ASSET/IMAGES/LARGE/CS-2013-003113_0014.JPEG.
[77] E. Díaz López, A. Comas-Vives, CO2 activation dominating the dry reforming of methane catalyzed by Rh(111) based on multiscale modelling, Catal. Sci. Technol. 13 (2023) 7162–7171, https://doi.org/10.1039/D3CY01546G.
[78] N.F. Khairudin, M.F.F. Sukri, M. Khavarian, A.R. Mohamed, Understanding the performance and mechanism of Mg-containing oxides as support catalysts in the thermal dry reforming of methane, Beilstein J. Nanotechnol. 9 (2018) 1162, https://doi.org/10.3762/BJNANO.9.108.
[79] S. Das, A. Jangam, S. Xi, A. Borgna, K. Hidajat, S. Kawi, Highly dispersed Ni/Silica by Carbonization-Calcination of a chelated precursor for Coke-Free dry reforming of methane, ACS Appl. Energy Mater. 3 (2020) 7719–7735, https://doi.org/10.1021/ACSAEM.0C01122/ASSET/IMAGES/LARGE/AE0C01122_0003.JPEG.
[80] M. Yusuf, M. Beg, M. Ubaidullah, S.F. Shaikh, L.K. Keong, K. Hellgardt, B. Abdullah, Kinetic studies for DRM over high-performance Ni–W/Al2O3–MgO catalyst, Int J. Hydrog. Energy 47 (2022) 42150–42159, https://doi.org/10.1016/J.IJHYDENE.2021.08.021.
[81] Y. Cui, H. Zhang, H. Xu, W. Li, Kinetic study of the catalytic reforming of CH4 with CO2 to syngas over Ni/α-Al2O3 catalyst: the effect of temperature on the reforming mechanism, Appl. Catal. A Gen. 318 (2007) 79–88, https://doi.org/10.1016/J.APCATA.2006.10.044.
[82] J. Han, Y. Liang, L. Qin, Y. Wang, H. Wang, F. Yu, B. Zhao, The reaction mechanism and its kinetic model of CO2 reforming with CH4 over Ni-Mg15@HC catalyst, Catal. Lett. 150 (2020) 1479–1488, https://doi.org/10.1007/S10562-019-03052-7/FIGURES/5.
[83] S. Wen, M. Liang, J. Zou, S. Wang, X. Zhu, L. Liu, Z.J. Wang, Synthesis of a SiO2 nanofibre confined ni catalyst by electrospinning for the CO2 reforming of methane, J. Mater. Chem. A Mater. 3 (2015) 13299–13307, https://doi.org/10.1039/C5TA01699A.
[84] C. Anjaneyulu, L.O.O.D. Costa, M.C. Ribeiro, R.C. Rabelo-Neto, L.V. Mattos, A. Venugopal, F.B. Noronha, Effect of zn addition on the performance of Ni/Al2O3 catalyst for steam reforming of ethanol, Appl. Catal. A Gen. 519 (2016) 85–98, https://doi.org/10.1016/J.APCATA.2016.03.008.
[85] S. Shoji, X. Peng, T. Imai, P.S. Murphin Kumar, K. Higuchi, Y. Yamamoto, T. Tokunaga, S. Arai, S. Ueda, A. Hashimoto, N. Tsubaki, M. Miyauchi, T. Fujita, H. Abe, Topologically immobilized catalysis centre for long-term stable carbon

dioxide reforming of methane, Chem. Sci. 10 (2019) 3701–3705, https://doi.org/10.1039/C8SC04965C.
[86] J. Guo, Z. Hou, J. Gao, X. Zheng, DRIFTS study on adsorption and activation of CH4 and CO2 over Ni/SiO2 catalyst with various ni particle sizes, Chin. J. Catal. 28 (2007) 22–26, https://doi.org/10.1016/S1872-2067(07)60009-6.
[87] L.F. Bobadilla, V. Garcilaso, M.A. Centeno, J.A. Odriozola, Monitoring the reaction mechanism in model biogas reforming by in situ transient and steady-state DRIFTS measurements, ChemSusChem 10 (2017) 1193–1201, https://doi.org/10.1002/cssc.201601379.
[88] K. Wang, M. Cao, J. Lu, Y. Lu, C.H. Lau, Y. Zheng, X. Fan, Operando DRIFTS-MS investigation on plasmon-thermal coupling mechanism of CO2 hydrogenation on Au/TiO2: the enhanced generation of oxygen vacancies, Appl. Catal. B 296 (2021) 120341, https://doi.org/10.1016/j.apcatb.2021.120341.
[89] Y. Zhang, Y. Zu, D. He, J. Liang, L. Zhu, Y. Mei, Y. Luo, The tailored role of "defect" sites on γ-alumina: a key to yield an efficient methane dry reforming catalyst with superior nickel utilization, Appl. Catal. B 315 (2022) 121539, https://doi.org/10.1016/j.apcatb.2022.121539.
[90] S. Zhang, M. Ying, J. Yu, W. Zhan, L. Wang, Y. Guo, Y. Guo, NixAl1O2-δ mesoporous catalysts for dry reforming of methane: the special role of NiAl2O4 spinel phase and its reaction mechanism, Appl. Catal. B 291 (2021) 120074, https://doi.org/10.1016/J.APCATB.2021.120074.
[91] M. González-Castaño, J. González-Arias, L.F. Bobadilla, E. Ruíz-López, J. A. Odriozola, H. Arellano-García, In-situ DRIFTS steady-state study of CO2 and CO methanation over Ni-promoted catalysts, Fuel 338 (2023), https://doi.org/10.1016/j.fuel.2022.127241.
[92] X.E. Verykios, Catalytic dry reforming of natural gas for the production of chemicals and hydrogen, Int J. Hydrog. Energy 28 (2003) 1045–1063, https://doi.org/10.1016/S0360-3199(02)00215-X.
[93] T. Rajkumar, A. Sápi, M. Ábel, J. Kiss, I. Szenti, K. Baán, J.F. Gómez-Pérez, Á. Kukovecz, Z. Kónya, Surface engineering of CeO2 catalysts: differences between solid solution based and interfacially designed Ce1−xMxO2 and MO/CeO2 (M = Zn, Mn) in CO2 hydrogenation reaction, Catal. Lett. 151 (2021) 3477–3491, https://doi.org/10.1007/S10562-021-03591-Y/FIGURES/11.
[94] C.J. Clark, Fast determination by Fourier-transform infrared spectroscopy of sugar–acid composition of citrus juices for determination of industry maturity standards, N. Z. J. Crop Hortic. Sci. 44 (2016) 69–82, https://doi.org/10.1080/01140671.2015.1131725.
[95] A. Omran, S.H. Yoon, M. Khan, M. Ghouri, A. Chatla, N. Elbashir, Mechanistic insights for dry reforming of methane on Cu/Ni bimetallic catalysts: DFT-Assisted microkinetic analysis for coke resistance, Catalysts 2020 10 (2020) 1043, https://doi.org/10.3390/CATAL10091043.
[96] T. Rajkumar, A. Sápi, M. Ábel, J. Kiss, I. Szenti, K. Baán, J.F. Gómez-Pérez, Á. Kukovecz, Z. Kónya, Surface engineering of CeO2 catalysts: differences between solid solution based and interfacially designed Ce1−xMxO2 and MO/CeO2 (M = Zn, Mn) in CO2 hydrogenation reaction, Catal. Lett. 151 (2021) 3477–3491, https://doi.org/10.1007/S10562-021-03591-Y/FIGURES/11.